University of Alberta

The Impingement of a Turbulent Wall Jet onto a Forward Facing Vertical Step

by

Douglas Christopher Langer 

A thesis submitted to the Faculty of Graduate Studies and Research in partial fulfillment of the requirements for the degree of

Master of Science

Department of Mechanical Engineering

Edmonton, Alberta
Fall 2008

Your file Votre référence
ISBN: 978-0-494-47288-0
Our file Notre référence
ISBN: 978-0-494-47288-0

For Anna

Abstract

This study examines a horizontal wall jet impinging onto a forward facing vertical step in a cross-flow. Planar laser induced fluorescence experiments in a water channel demonstrate that the wall jet becomes a vertical elliptical jet after impinging on the step. A predictive empirical model was created using perimeter and aspect ratio measurements of these elliptical jets. The feasibility of using computational fluid dynamics for this geometry was determined through the use of a solver for the RANS equations with a k-ϵ closure model. The trajectory of the jet was measured and fit with power-law relationships with exponents of 1/2 (near field) and 1/3 (further downstream). The use of modified round jet entrainment models demonstrated that momentum losses caused by the jet-step interaction could be represented by a shape change and a drag force with a coefficient of 1.6.

Acknowledgements

I would like to thank my supervisors Dr. Brian Fleck and Dr. David Wilson for their support and assistance during my graduate program. I am also thankful to the Natural Sciences and Engineering Research Council of Canada for the funding of my research. Thanks to Luis Torres for his help with the water channel facility, the PLIF system, LaTeX, and for his perspective. I would also like to thank my family for their support throughout my entire educational experience. Lastly, thanks to Anna for talking me through difficult times and for always being there.

Contents

1 Introduction **1**

1.1 Motivation 1

1.2 Scope 3

1.3 Background 3

1.3.1 Wall Jet 4

1.3.2 Impinging Jet 5

1.3.3 Jet in Cross-Flow 6

1.3.4 PLIF 11

1.3.5 CFD 13

1.4 Objectives 15

1.5 Outline 16

2 Experimental Method **17**

2.1 Experimental Facility 17

2.2 Test Section 18

2.3 Measurement System 20

2.3.1 Light Source 20
2.3.2 Dye 21
2.3.3 Imaging System 22
2.3.4 Calibration Procedure 23
2.4 Aspect Ratio Measurements 26
2.5 Jet Trajectory Measurements 28

3 Crater Region **37**

3.1 Introduction 37
3.2 CFD Constraints 38
3.2.1 Geometry 38
3.2.2 Perimeter Measurement Method 46
3.3 PLIF Results 46
3.4 Discussion 47
3.4.1 Empirical Perimeter Correlation 47
3.4.2 Experimental Aspect Ratio Correlation 49
3.4.3 Comparison of CFD to Experimental Data 49
3.5 Conclusion 51

4 Jet in Cross-Flow Region **69**

4.1 Introduction 69
4.2 Empirical Correlations 70
4.3 Entrainment Model 74
4.4 Conclusion 80

5 Conclusion **100**

5.1 Summary 100

5.2 Future Work 101

A Appendix - Rotameter Calibration **110**

B Appendix - Elliptical Jet Model **112**

C Appendix - Derivation of Equation 4.9 **118**

D Appendix - L_o Independence in Trajectory Correlations **122**

List of Tables

3.1 Effect of residual on CFD measurements 57

4.1 Elliptical entrainment coefficient β_e 99

B.1 Effect of S on β_e and jet trajectory 117

List of Figures

2.1 Water Channel Schematic 29

2.2 Turbulence Generator Schematic 30

2.3 Test Section Schematic 31

2.4 Laser sheet optics schematic 32

2.5 Aspect ratio measurement schematic 33

2.6 Jet trajectory measurement schematic 34

2.7 Isometric view of jet impingement 35

2.8 Elliptical fit 36

3.1 Test section schematic 52

3.2 CFD dimensions 53

3.3 CFD boundary conditions 54

3.4 CFD mesh 55

3.5 Blending factor ϕ 56

3.6 Single image concentration profile 58

3.7 Concentration along the maximum depth line 59

3.8 Concentration along the maximum width line 60

3.9 Measured perimeter compared with L 61

3.10 Measured perimeter compared with H 62

3.11 Measured perimeter compared with R 63

3.12 Linear fit of perimeter model 64

3.13 Linear fit of aspect ratio model 65

3.14 Experimental and CFD concentration profiles 66

3.15 Comparison of CFD to experimental results for perimeter 67

3.16 Comparison of CFD to experimental results for aspect ratio 68

4.1 Single jet trajectory image 82

4.2 Average jet trajectory contours 83

4.3 Empirical curve fits for trajectories 84

4.4 Near-field trajectory fits 85

4.5 Determination of B_1 86

4.6 Bent-over jet trajectory fits 87

4.7 Determination of B_2 88

4.8 Recirculation zone 89

4.9 Definition of R^* 90

4.10 Entrainment modeling assuming round jet 91

4.11 Effect of jet shape on entrainment model prediction 92

4.12 Effect of drag and entrainment below step on model prediction 93

4.13 Effect of velocity ratio on drag coefficient 94

4.14 Effect of step geometry on drag coefficient 95

4.15 Entrainment coefficient α 96

4.16 Entrainment coefficient β 97

4.17 Curve fits using entrainment model 98

A.1 Rotameter calibration curve 111

C.1 Control Volume for Derivation of Equation 4.9 121

List of Symbols

Symbols:

α	Entrainment coefficient with a theoretical value of 0.11
β	Entrainment coefficient with a theoretical value of 0.6
β_e	Elliptical entrainment coefficient
δ	Boundary layer thickness
γ	GCI Ratio
ν	Fluid viscosity
ϕ	Blending factor in CFD code
ρ	Density
A	Area of jet
B_1	$x^{1/2}$ power law fit coefficient
B_2	$x^{1/3}$ power law fit coefficient
d	Diameter of initial round jet
D	Minor axis of the elliptical cross section
h	Height above step

H Step height

ℓ_m Momentum length scale

L Distance from jet to step

L_o Distance from an equivalent point source to step

p Order of accuracy of CFD code

P Perimeter of elliptical jet

r Grid refinement ratio

R Ratio of the mean velocity of the jet exiting the pipe compared with the mean cross-flow velocity

R^* Ratio of the calculated velocity of the vertical jet entering the cross-flow to the local cross-flow velocity ratio at the top of the step

S Jet aspect ratio

t Boundary layer travel time

U_∞ Cross-flow velocity

V Velocity

V_{jet} Jet velocity

V_∞ Cross-flow velocity

w_o Velocity of vertical jet emitted into cross-flow

x Distance from the vertical jet source

z Height from the floor of the waterchannel

Abbreviations:

CFD	Computational Fluid Dynamics
GCI	Grid Convergence Index
PLIF	Planar Laser Induced Fluorescence

Chapter 1

Introduction

1.1 Motivation

The study of turbulent jets is applicable to a wide variety of industrial applications ranging from mixing within an engine to the dispersion of pollutants from a smokestack. This diversity of possible flow phenomena has inspired the study of many different geometries and configurations of jets over the past several decades. Each phenomena's individualized characteristics must be understood before the flow can be used or modelled for engineering applications.

The behaviour and characteristics of jets can be predicted through the study of fundamental fluid mechanics. These predictions can lead to improved safety in the case of vented pollutants or better mixing in industrial processes.

Underground pipelines can carry high concentrations of dangerous fluids such as sour

gas or natural gas. Occasionally these pipes fail, leading to the release of significant quantities of toxic or flammable gasses. The rupture of a buried pipe produces a crater, where the gas is released at high velocities and impinges onto the crater wall. The interactions between the jet and the crater lead to significant spreading and momentum losses in the jet which can drastically change the rate of dilution of the released gases in the surrounding air. These ruptures can produce significant ill-effects to the environment and danger for the populous surrounding the rupture area. The ability to model the concentration distributions of the pollutant within the atmosphere allows for safe placement of toxic gas pipelines and proper emergency response in the event of a poisonous gas release [1].

Previous studies [2, 3] have determined the properties of the plume issued after a pipeline rupture using existing plume dispersion models. These studies primarily examined the pressure and Mach number effects on plume behavior and assumed the jet exited the crater as a round jet with momentum losses caused by a drag force with a drag coefficient of 1.0. These studies recommend a series of experiments to measure this drag coefficient. While their assumptions seem plausible, further research on the effects of the crater on the downstream plume is required. It is the aim of this study to provide further information on the jet-crater interaction, which can be used in hazard assessment models to more accurately predict the behavior of the jet.

1.2 Scope

This research examines a simplified version of a ruptured underground pipeline release which is composed of a turbulent wall jet impinging onto a vertical forward-facing step in a cross-flow. This simplification removes the effects of the back and side walls of the crater, allowing the effect of the impingement to be studied directly. The analysis of the jet consisted of two parts: the 'crater' region consisting of the wall jet and its impingement, and the 'jet in cross-flow' region above the step. Two measurement locations were chosen to define each region. The 'crater' region was studied by measuring the perimeter and aspect ratio of the jet issuing vertically into the cross-flow in the plane of the top of the step. The jet's penetration was determined by jet trajectory measurements made along the jet's centerline in the 'jet in cross-flow region'. These measurements were used to characterize the flow and models were subsequently developed to replicate the measurements in these locations.

1.3 Background

This specific flow configuration has received very little attention in the literature due to its complexity, however, it can be broken into components which have been extensively researched. There are three primary regions within the jet which have been presented in the literature: the wall jet (representing the flow of the jet along the floor prior to the impingement), the impinging jet, and the jet in cross-flow. A brief explanation of each region provides an idea of the actual flow structures as well as the simplifications used in the creation of the models. A summary of the theory behind the planar laser induced

fluorescence (PLIF) system used for the experimental measurements is also provided. Lastly, the use of computational fluid dynamic (CFD) modeling for jets is discussed.

1.3.1 Wall Jet

An excellent description of the physics of the wall jet is provided by Launder and Rodi [4], who review the prior research on this geometry. The wall jet is defined as "a shear flow directed along a wall where, by virtue of the initially supplied momentum, at any station, the stream-wise velocity over some region within the shear flow exceeds that in the external stream" [4]. For the sake of simplicity, a 'wall jet' will be defined here as a round jet issuing parallel to a wall issued at various heights above the wall. As the jet interacts with the wall, the initial Gaussian velocity profile of the jet is lost. The ratio of the location of the maximum velocity to the jet half-width was found to be 0.15 [4]. Far from the wall, the jet's velocity profile resembles that of a free jet. This produces a velocity profile with a maximum near the wall and a long tail far from the wall. The losses of jet momentum which cause this change in the velocity profile were incorporated into a drag coefficient. This drag coefficient and a uniform velocity profile were assumed for the development of the entrainment models presented in this study.

The spreading rates for wall jets are of particular interest in the study of the impinging wall jet, as the shape and size of the impinging jet is dependent on the spreading of the wall jet. Experimental data and simulations showed that the jet half width grows at a rate of approximately 0.065 times the distance from the jet [5]. The jet's horizontal spread was found to be 0.32 times the distance from the jet [5], which is significantly more than the

vertical spread of the jet. This shows that the wall jet has a cross-section with an aspect ratio that increases with the distance the jet travels along the wall. Thus, it should be expected for the present work that at the time of impingement at the step, the initially round jet will have an aspect ratio whose value is dependent on the distance traveled along the wall.

Davis and Winarto [6] studied the growth and the turbulence of a wall jet at different heights from the ground. Because of the initial displacement, the jet started as a free jet which after spreading, transitioned to a wall jet. They found that increasing the height of the jet from the floor lead to the apparent origin of the fully developed wall jet to move further behind the nozzle exit. This shows that for the pipeline rupture scenario the depth of the crater relative to the location of the jet may have an effect on the total spreading of the jet. To simplify the problem for this study, this effect was neglected and the jet was mounted flush with the ground.

1.3.2 Impinging Jet

The turbulent jet impinging onto a flat surface has been well documented in the literature due to its importance in heat transfer applications. The interaction between the jet and the wall is primarily governed by inviscid relationships and is dependent more on pressure forces than turbulence [7, 8]. A detailed analysis of the impinging jet under several different conditions is given by Donaldson and Snedeker [8]. When analyzed, the impinging jet is typically broken into three regions: the free jet region, the impingement region, and the wall jet region [9, 10]. Prior to impingement, the jet grows as a free jet from the nozzle

towards the impingement surface. The jet experiences the pressure effects caused by the wall as the flow enters the impingement or stagnation region. There, the jet's axial velocity drops to zero and the jet's momentum spreads radially and symmetrically. A detailed analysis of the turbulence statistics within this region is given by Nishino et al. [11]. The flow that issues from the stagnation region is a radial wall jet with a velocity profile similar to that of the standard wall jet case with a maximum velocity near the wall [10, 12]. Song and Abraham [12] demonstrate that the impinging jet has less momentum than an equivalent radial wall jet due to the pressure and friction losses. The impingement causes the jet's shape to change by flattening it against the wall and spreading it radially. The amount of radial spread is dependent on the size of the plate on which the jet impinges. It will be shown that for the entrainment model, the effect of this impingement can be represented by a momentum loss (characterized by a drag force) and a change in the jet's shape.

1.3.3 Jet in Cross-Flow

The jet in cross-flow region is of particular interest because it shows the dilution of the released pollutant. The shape, size, and location of the plume determine the location and concentration of the released gasses. Significant research has been performed in this field because of its importance in pollutant dispersion and the rapid mixing required in combustion applications. The round jet and the elliptical jet will be discussed in this section, as well as a method of predicting jet trajectories through entrainment modelling.

Round Jet

The round jet in cross-flow has received significant attention in the literature because of its wide range of applicability ranging from pollution dispersion (smokestacks) to fuel injection (in engines or industrial burners). The most interesting factor in the study of the round jet is its trajectory, which determines the dispersion of the pollutant. A detailed summary of the round jet in cross-flow is given by Margasson [13]. A summary of the various scaling factors and recent work on the round jet in cross-flow is given by Muppidi and Mahesh [14].

The definition of the jet's trajectory depends on the measurement techniques used in the study. The trajectory is typically defined to follow either the maximum scalar concentration [15], the maximum velocity contours [16], or the mean jet streamlines [17]. The jet penetration measured by these methods has been shown to vary by approximately 5-10 percent, with the maximum velocity method predicting the highest values of penetration [14]. The use of the maximum scalar concentration slightly underpredicts the jet's trajectory due to the counter-rotating vortex pair within the jet drawing fluid (and scalar) from the top of the jet to the bottom [17]. This study uses the maximum scalar concentration to define the jet's trajectory since the scalar concentration was measured directly using the PLIF method. This method is commonly used in the literature, especially in experimental studies where scalar concentrations can be measured directly.

Round jet in cross-flow trajectories have been modelled using different scaling factors which are outlined by Muppidi and Mahesh [14] (summarized here). The models show that

the jet to cross-flow velocity ratio (for constant density flows), which represents the square root of the momentum ratio of the plume to the cross-flow, is the key factor in determining the penetration of the jet [14]. In the literature, three scaling factors which are used to normalize the jet's height and position are: the jet diameter (d), the velocity ratio multiplied by the diameter (Rd), and the square of the velocity ratio multiplied by the diameter (R^2d). Smith and Mungal [15] showed that the best scaling factor for the round jet in cross-flow is Rd. From this, the far field trajectories can be represented as a power law with an exponent which ranges from 0.28 to 0.34 depending on the study [13]. Broadwell and Breidenthal [18] and Weil [19] show that the near field of the jet can be modelled using a power law with an exponent of 1/2 and the far field with an exponent of 1/3. Using these scalings, round jet trajectories can be accurately represented by a single function. A scaling factor and power law fit is provided later for the impinging wall jet.

Elliptical Jet

In this work, the shape of the jet above the step is roughly elliptical in nature with a high aspect ratio (> 10). The elliptic jet in cross-flow has received less attention than the round jet in cross-flow in the literature due to the increased complexity caused by the asymmetries in the flow. The vortex structures differ greatly between the round and elliptic jets [20]. The high aspect ratio jets experience vortex pairing on the upwind side of the plume which alters both the entrainment and the structure of the jet [21]. Due to these differences, unlike the round jet, simple scalings do not directly allow the elliptical trajectories to be represented by a single function [22]. Lim et al. [22] found some collapse with Rd_h (where d_h is

the hydraulic diameter of the jet), however the collapse deteriorated with increasing aspect ratio. As only limited study has been undertaken on elliptical jets in cross-flow, and none could be found with aspect raitos greater than five, round jet theory was modified to create the models for the trajectory of the jet above the step. The findings from the elliptical case showed that full collapse of the data was not available. As such, it was assumed that the curve fits and models produced to describe the flow studied in this work would be more dependent on the initial flow conditions than the round jet.

Entrainment Modeling

The rate of dispersion of pollutants released from pipeline ruptures is primarily dependent on the plume's trajectory. The maximum plume rise is used to aid in the dillution process of pollutants [19]. Significant work on round jets issuing into cross-flows in the form of smokestacks can be seen in the literature. Simplified entrainment models have been presented [19, 23, 24] which assume that "the rate of ingestion of ambient air into a plume is proprtional to an inflow or entrainment velocity at the plume edge" [19]. This entrainment velocity is proportional to the plume velocity, with an entrainment constant which is dependent on the flow geometry [19]. With this assumption, the equations for conservation of mass and momentum can be solved directly to give predicitions of mean jet trajectories. Detailed derivations of these predictive equations are given by Briggs [23]. The solution predicts two regions, an initial region where the plume is dominated by its initial momentum (represented by a 1/2 power law) and a bent over region (represented by a 1/3 power law) [19]. In these two regions, the power law fits were determined analytically through

solving the governing conservation equations by making simplifying assumptions. In the near field region, it was assumed that the initial velocity of the jet dominated its trajectory, and the jet was travelling vertically. In this situation the jet velocity V_{jet} was assumed to be much greater than the cross-flowing velocity V_∞. In the fully bent-over region, it was assumed that the jet had entrained so much of the surrounding fluid that the jet's momentum was dominated by the horizontal velocity of the cross-flowing fluid. Through the use of these assumptions, several terms of the conservation equations were deemed negligible (since $V_{jet} << V_\infty$ or $V_{jet} >> V_\infty$), allowing for analytic solutions to the equations. This produced the power law fit solutions to the entrainment models presented by Briggs [23].

The entrainment coefficient (β), representing the spreading rate of the jet (with radius b), is defined in equation 1.1 [23]. For a round jet in cross-flow, β was found to have an average value of 0.6 [23]. These models rely heavily on the ratio of the initial velocity of the jet exiting the smokestack to the cross-flow velocity. It will be shown that the momentum loss, which occurs before the step, can be approximated by a drag force. Using the shape of the jet exiting the step and the drag coefficient, a reasonable approximation for the vertical jet velocity ratio can be determined. This velocity ratio can then be used to predict the trajectory of the elliptical jet using entrainment models.

$$\beta = \frac{db}{dz} \tag{1.1}$$

1.3.4 PLIF

Planar laser induced fluorescence is a measurement technique which allows the concentration of a scalar to be measured across a plane through the use of fluorescence. When fluorescent dyes are exposed to photons, valence electrons are excited to a higher energy state after which they fall back to their ground state, releasing a photon [25]. Since energy is lost in this process, the emitted light is at a different wavelength than the light used for excitation. For the sake of sodium fluorescein (used in this study), the peak absorption lies at a wavelength of 488 nm (conveniently one of the bands of the Argon laser) and the emission peak is at 515 nm [26]. Because the absorption and emission bands are at different wavelengths, filters can be used to remove the excitation light, allowing direct measurement of the fluoresced light. As photons are used for excitation, they are lost from the laser beam, lowering its intensity through attenuation. The effects of laser beam attentuation are most noticable at high dye concentrations, but are negligible for the concentrations used in this study [25]. The fluorescent intensity is linearly dependent on both the concentration of the dye and the laser intensity [25]. Through proper calibration, the effect of the laser intensity can be removed, leading to concentration measurements in the fluid. The fluorescence intensity and spectrum of fluorescein also changes with the pH of the surrounding fluid due to changes in the structure of the dye [27]. The intensity increases up to a pH of 8 then drops off [28]. The fluorescent intensity is also dependent on temperature [25]. These effects are minimized by using the same temperature and pH of the water for both the measurements and the calibration. Thus, through controlling the temperature and pH of the flow being measured, concentration measurements within the fluid can be taken in a non-intrusive manner.

In some cases, the excited electron falls to the triplet state where it is "vulnerable to chemical or physical quenching" and can be irreversibly converted to a compound which is no longer fluorescent through a process called photobleaching [29]. The level of photobleaching is dependent on the power of the laser and the residence time of the dye in the beam [29]. Due to its solubility and absorption level of the 488 nm light emitted by the Argon laser, sodium fluorescein is more strongly affected by photobleaching than other dyes [30]. This effect is minimized by the spreading of the laser (leading to lower intensity at each location), and in most fluid dynamics studies (especially those of turbulent flows) the time each particle spends in the beam and the intensity of the laser light at any point is sufficiently small that photobleaching is insignificant [29].

The LIF technique can be used to measure the concentrations of single points, lines, planes (PLIF), or volumes [30]. This study focuses on planar measurements which require illumination through the use of a laser sheet. Beam scanning [31] and the use of optics [29] are the two primary methods of producing laser sheets. Beam scanning systems use triggers to ensure that each time the shutter of the camera is opened the beam travels through the entire measurement volume. Optics can also be used to spread the beam producing a constant sheet of light. Light is typically spread by a cylindrical lens which produces a Gaussian intensity profile within the sheet, however, a Powell lens can be used which produces an approximately uniform intensity profile [32]. Due to its inherent simplicity and uniform velocity profile over large regions, a Powell lens system is used in this study.

1.3.5 CFD

In many cases, experimental results for specific geometries are not available in the literature or cannot be created in a laboratory setting. In these cases, a computer simulation can be used to predict the flow behaviour. Computational fluid dynamics (CFD) are used to determine the behaviour of fluids through solving the Reynolds Averaged Navier Stokes (RANS) Equations. However, the RANS equations do not represent a closed model and closure models are required to determine the Reynolds stress tensor and fully define the flow [33]. Three main types of closure models are used for engineering applications: two-equation eddy-viscosity models, differential Reynolds-stress equation models, and hybrid models [34]. Two-equation models are the simplest and most robust models and are the most computationally inexpensive [33]. Differential Reynolds-stress equation models offer higher accuracy but significantly more computational cost [34]. Since this study examines the feasibility of using CFD to predict a series of different conditions, a two-equation model (k-ϵ) was used because of its robustness and speed of convergence.

The standard k-*epsilon* model uses the turbulent viscosity hypothesis which assumes that the "deviatoric Reynolds stress is proportional to the mean rate of strain" [33]. The turbulent viscosity (ν_T), kinetic energy (k) and dissipation (ϵ) solved in this model are given in Equations 1.2 to 1.4. The standard k-ϵ model uses the constants: $C_\mu = 0.09$, $C_{\epsilon 1} = 1.44$, $C_{\epsilon 2} = 1.92$, $\sigma_k = 1.0$ and $\sigma_\epsilon = 1.3$ [35].

$$\nu_T = \frac{C_\mu k^2}{\epsilon} \tag{1.2}$$

$$\frac{\bar{D}k}{\bar{D}t} = \nabla \cdot \left(\frac{\nu_T}{\sigma_k} \nabla k \right) + \wp - \epsilon \tag{1.3}$$

$$\frac{\bar{D}\epsilon}{\bar{D}t} = \nabla \cdot \left(\frac{\nu_T}{\sigma_\epsilon} \nabla \epsilon \right) + C_{\epsilon 1} \frac{\wp \epsilon}{k} - C_{\epsilon 2} \frac{\epsilon^2}{k} \tag{1.4}$$

Due to the simplifications involved in the above equations, there are several inherent inaccuracies within the k-ϵ model [33]. Hanjalić [34] presents a detailed explanation of the shortcomings of the k-ϵ turbulence model both in theory and compared to experimental results. For example, these inaccuracies can lead to over-prediction of the turbulent kinetic energy, and result in an overprediction of the spreading of simulated jets [36]. This additional spreading can be shown through analyzing the boundary layer thickness (δ) for a laminar boundary layer along a wall.

$$\delta = \frac{5 x^{1/2} \nu^{1/2}}{V_\infty^{1/2}} \tag{1.5}$$

A travel time t can be defined as:

$$t = \frac{x}{V_\infty} \tag{1.6}$$

Substituting this into equation 1.5 yields:

$$\delta = 5\sqrt{t\nu} \tag{1.7}$$

For a given travel time,

$$\delta \propto \sqrt{\nu} \tag{1.8}$$

So, as the viscosity increases, the spreading of the boundary layer increases. In the case of the jet travelling on the floor, the artificial viscosity created in the CFD model leads to an increase in the viscosity of the flow and thus increases the predicted spreading of the jet.

Despite the inaccuracies, the k-ϵ model is commonly used in industrial applications as it gives reasonable trend and order of magnitude flow predictions. This model has been used in many types of flows such as swirling jets [36], slot jets in cross-flow [37], and wall jets [38]. In cases where several flow conditions are to be tested (such as the parametric study presented in this work) the simplest model requiring the least amount of computational time is the most desirable. The uncertainties in the CFD measurements used here were analysed using the method presented by Roache [39] and are discussed in detail later. Despite the uncertainty in the CFD modelling, the k-ϵ model provided reasonable predictions and is a feasible means of predicting the flow.

1.4 Objectives

The objective of this research is to examine the behavior of a turbulent wall jet impinging onto a forward facing step in a cross-flow. This work provides insight into the behavior of fluids released from underground pipeline ruptures through studying the effects of the impingement of the released fluid onto the crater surrounding the ruptured pipe. From this analysis, a predictive model can be derived and incorporated into hazard assessment models for pipeline ruptures. The following specific objectives are used to fully define this study:

- Produce predictive models for the shape of the jet entering the cross-flow, and the trajectory of the jet in the cross-flow. These models are to be based entirely on the inlet conditions such as the location and size of the step, and the initial jet and cross-flow velocities so that no jet measurements are required to predict the jet's behavior.
- Using ANSYS-CFX, determine the feasibility of using a simple numerical model for predicting the flow of the jet.
- Determine how the jet trajectory can be modeled by modifying existing entrainment models for round jets in cross-flow.

1.5 Outline

This chapter has outlined the motivation for studying this geometry, and provided appropriate background information for this topic. Chapter 2 provides detailed information about the specific equipment used and the general set-up of the experiments. Information on how the experiments were performed is also given in Chapter 2. Chapter 3 examines the 'crater-region' of the jet consisting primarily of the measurements of the jet issuing vertically from the step into the cross-flow. The computational study and the empirical correlations evaluating the shape and size of the vertical elliptic jet are also presented. Chapter 4 examines the 'jet-in-cross-flow region' through the use of emperical curve fits and entrainment modelling. Chapter 5 summarizes the major conclusions from this work and outlines areas recommended for future study.

Chapter 2

Experimental Method

2.1 Experimental Facility

Tests were performed in a 5000 L recirculating water channel at the department of Mechanical Engineering at the University of Alberta [40, 41, 42]. A schematic of the water channel is shown in Figure 2.1. The system consisted of a 5.24 m long glass channel with a rectangular cross section measuring 47 cm by 68 cm which allowed optical access from both sides and the top of the channel. For the experiments performed in this study, the depth of water in the channel was maintained at 40 cm, with a flat glass panel placed at the top of the test section to minimize the optical effects caused by the free water surface. Two centrifugal pumps with variable outlet diameters were used to control the velocity of the cross-flow, which was varied from 0.041 m/s to 0.081 m/s, producing Reynolds numbers (based on hydraulic diameter) ranging from 2×10^4 to 4×10^4. The flow traveled through turning vanes and two metal screens before a contraction into the channel and a final flow straightener. The flow within the channel was identical to the turbulent boundary layer

shear flow used by Hilderman [43] which was created through the use of a grid and a saw-tooth trip fence. The dimensions and locations of the turbulence generating equipment is shown in Figure 2.2. The turbulent boundary layer then developed along roughness elements consisting of a 12.7 mm diamond shaped steel mesh attached to acrylic panels placed on the floor along the length of the channel. Measurements were made [43] using a two component LDA at the test location, approximately 3 m from the channel inlet (without the step in place). These measurements found that the flow formed a log-law boundary layer with a profile that could be approximated as:

$$U = \frac{u_*}{\kappa} ln\left(\frac{z-d}{z_0}\right) \tag{2.1}$$

"where $u_* = 14$ mm/s is the friction velocity, $\kappa = 0.4$ is the Von Karman constant, $d = 1.7$ mm is the zero-plane displacement height, and $z_o = 0.52$ mm is the roughness height" ([43], p.15). This gives an approximation for the velocity profile of the cross-flow used in this study. The boundary layer thickness δ in the jet exit plane at the measurement location was found to be 15 mm. The presence of both the jet tube and the flow contraction caused by the step altered the cross-flow velocity profile, however this gives an accurate representation of the flow entering the test section.

2.2 Test Section

The test section, where the experimental measurements were taken, was located 3 m from the channel inlet and consisted of the jet tube and the step. The orientation of the jet

and step as well as the variables changed in the parametric study are shown in Figure 2.3. The step consisted of a 1.2 m long sheet of 12.7 mm thick acrylic painted black to reduce reflections. The height of the step was adjusted by adding strips of 12.7 mm thick acrylic at three locations below the sheet. This allowed three measurement heights: 2.54, 3.81, and 5.08 cm. For each height, the impingement surface of the step was sealed using black tape to ensure that it was smooth and flat, and to minimize the seepage of jet fluid underneath the step. The step was located at three distances from the pipe: 5, 9, and 15 jet diameters (43.75, 78.75 and 131.25 mm respectively).

The jet emitted from an 8.75 mm diameter (d), 1 m long brass pipe attached to the floor of the channel. The pipe consisted of the jet tube and turbulence generator used by Johnston and Wilson [42] with a 1 m extension tube attached to the end. The extension tube ensured that the vertical inlet tube did not significantly effect the cross-flow and that the flow profile in the pipe was fully turbulent. The pipe was centered and mounted flush with the grid on the bottom of the channel. The tube connected to a bent pipe and attached to a 75 L pressure vessel which was maintained at a constant pressure of 2.1 bar. A needle valve and a rotameter were used to control the flow of jet fluid. Three jet velocities were used: 0.47, 0.78, and 1.1 m/s resulting in Reynolds numbers based on jet diameter ranging from 4.1×10^3 to 1.0×10^4. The long development region (>100 jet diameters) and the Reynolds numbers used indicate that throughout the range of velocities, the pipe flow had a turbulent velocity profile.

2.3 Measurement System

Concentration measurements were taken using a planar laser induced fluorescence (PLIF) system developed at the water channel facility. The PLIF system used a light source (in the form of a laser sheet), a fluorescent dye with significantly different absorption and emission peaks, and a camera system capable of viewing the emitted fluorescent signal. Using this equipment, measurements of concentration could only be made if a calibration scheme was used which took into account the non-uniformities of the laser sheet, the CCD array variability, and other imperfections in the system. Images were then translated into concentration profiles through the use of processing software. These components are discussed below.

2.3.1 Light Source

The system used a 4 W Coherent Innova 70 Argon Ion laser running in single line mode at 488 nm with a rated power output of 2.1 W. The beam exiting the laser was steered through a series of optics to form a thin laser sheet in the water channel. The beam first traveled through a converging lens with a focal distance of one meter (the approximate length of the beam path from the lens to the center of the water channel). This lens minimized the thickness of the laser at the center of the water channel, producing a beam with a diameter of approximately 1 mm at the center of the water channel. The beam then traveled through two steering mirrors and an aperture which directed the beam onto a Powell lens with a divergence of 30°. The aperture minimized back reflections from the optics and the water channel. The Powell lens spread the beam into a laser sheet with an approximately uniform

intensity profile [32]. Cylindrical lenses are often used for laser sheet production, however they produce a Gaussian light distribution, which was found to produce a laser sheet of too narrow a width to be particularly useful for the large areas required in these experiments. The position of the optics used to form the laser sheet is shown in Figure 2.4.

2.3.2 Dye

Fluorescein Sodium Salt ($C_{20}H_{10}Na_2O_5$) from Fisher Scientific (A833-500) was used as the scalar tracer for the PLIF system. Dye was mixed uniformly in the jet fluid reserve tank at a concentration of 0.2 mg/L. The peak of the absorption curve for fluorescein dye occurs at 488 nm, while the emission peak is at 515 nm [26]. The effect of concentration on fluorescence intensity is linear and the effect of attenuation is negligible for low dye concentrations [25]. For the study used here, the maximum measured dye concentration within the laser sheet was 1.6×10^{-7} mol/L which occurred over a small area in the jet shape measurement locations. The average dye concentration along the laser path length (20 cm within the measurement location) was 6.6×10^{-8} mol/L. From this, the effect of laser attenuation was found to cause an error of approximately 10 percent in the concentration measurements [25]. The intensity of the fluorescence was found by Walker [25] to be highly dependent on pH and slightly dependent on the temperature of the carrying fluid. Because of the effects of the surrounding fluid on the fluorescence intensity, water channel fluid was mixed with the dye for both the jet and the calibration process to ensure the temperature and pH of the jet was identical to the cross-flowing fluid. This ensured that changes in intensity were due only to the concentration and the laser sheet intensity profile.

The calibration procedure outlined in Section 2.3.4 exploits the linear response of the dye to concentration and light intensity in order to convert intensity measurements to concentrations.

In order to produce accurate calibration images, known concentrations of the fluorescein were passed through the calibration tube and imaged. The fluid exiting the jet tube also had a known concentration of dye which was created by first dissolving a known mass of dye powder into water. This master solution was typically made with 100 mg of dye measured on a scale with 2 mg accuracy which was dissolved into a 1 L $\pm$ 5% Erlenmeyer flask and stirred using a mechanical stirrer to ensure the powder completely dissolved. This master solution was covered to minimize any photo-bleaching in the dye. The master solution was further diluted by taking a portion of the fluid (80 $\pm$ 0.6 mL for the jet and 15 $\pm$ 0.6 mL for the calibration tank) and mixing it into either the jet tank (40 $\pm$ 2 L) or the calibration tank (50 $\pm$ 2 L). This lead to an approximate uncertainty in the dye concentration of approximately 8 percent.

2.3.3 Imaging System

The imaging system was composed of a Cooke SensiCam camera (S/N: 370 KD 2267), a 75 mm Cosmicar TV Zoom Lens, and a Kodak wratten number 12 gelatin optical filter. For the jet area measurements, the camera was located 1.35 m above the step, and oriented perpendicularly to the surface of the water as shown in Figure 2.5. For the jet trajectory measurements, the camera was positioned 1.3 m from the center of the water channel, and

oriented perpendicularly to the side wall of the channel as shown in Figure 2.6. The zoom lens was focused using a ruler located in the water channel at the measurement location, giving a resolution of 0.25 mm/pixel for the area measurements and 0.27 mm/pixel for the jet trajectory measurements. The filter was used to eliminate any reflected laser light, and to ensure that the light entering the camera was produced entirely by the fluorescent dye. All light with a wavelength shorter than 500 nm was effectively attenuated and approximately 25 percent of the light at 515 nm (the emission peak of the dye) was transmitted [44]. This completely eliminated the 488 nm light from the laser, allowing only the light emitted from the fluorescein to pass to the CCD. During image acquisition, the room was darkened to ensure that there was as little background light as possible within the transmitting range of the filter. This ensured that the signal measured by the CCD was composed only of the ambient background light (which was removed during processing) and the light emitted by the fluorescent dye.

2.3.4 Calibration Procedure

The calibration of the PLIF system was developed at the water channel facility. The intensity of the laser sheet was not constant within the measurement location due to: the spreading of the laser, the profile caused by the Powell lens [32], the operating mode of the laser, the heterogeneity of the CCD, and other minor imperfections in the optics. Due to this non-uniform light intensity, a mathematical calibration, like that used by Hilderman [43], was nearly impossible. Instead, an experimental method was devised involving a square glass tube circulating known dye concentrations to produce an empirical calibration. This calibration allowed the fluorescent intensity measured by the camera to be converted

into an empirical measurement of the dye concentration. A 50 L calibration tank was used to hold known concentrations of dye mixed with water channel fluid (to avoid the effects of temperature and pH on the measurements). The large volume of this tank minimized the effects of photo-bleaching on the calibration process. The dyed water was fed through flexible tubing and circulated using a pump through a 2.5 cm square glass tube, which was assumed to have a linear transmissivity. The glass tube was then placed in the laser sheet so that the camera could record the intensity of the known concentrations of dye. Since the fluorescence intensity of the dye is linear with concentration [25], a three point calibration could be used to determine the linear calibration curve for each pixel. Three calibration values were used: 0 mg/L (background concentration with no square tube), 0.03 mg/L, and 0.06 mg/L. A jet concentration of 0.2 mg/L was used because at the measured locations, the jet was typically diluted to a concentration less than 0.06 mg/L. This lead to a maximum fluorescence intensity which approached the maximum allowable intensity for the camera (4095 digital counts), minimizing the effects of the background noise (which ranged from approximately 20-100 digital counts). At each calibration intensity, the maximum permissible intensity was determined by placing the square tube at the location nearest to the laser which could be seen by the camera. This set-up removed any reflections from bubbles or surfaces which might have had higher intensity than that produced by the dye. Since the beam was constantly spreading, the minimum intensity was located at the back of the water channel (the furthest location from the laser within the camera's view). This minimum intensity was also measured to remove any background light from the calibration images. After the maximum and minimum intensities were found, the square tube was traversed across the laser sheet at both concentrations (0.03 and 0.06 mg/L) to determine the coef-

ficients of the linear calibration curves for each pixel. Each traverse was composed of 1000 images, while the maximum and minimum values used 500 images. Measurements from the traverse were compared to the minimum and maximum concentrations and the pixels with measurements outside of this range were removed. The remaining values were averaged to determine the relationship between intensity and concentration for each pixel of the camera in the laser sheet. Experiments demonstrated that the intensity of the laser remained constant (within 2 percent) over the course of a day (after approximately 20 minutes of warm-up), so the calibration procedure was done once before each set of experiments. Due to the build-up of dye in the water channel, the background concentration was taken before and after each experiment for subtraction from the signal. It was found that the background build-up was typically less than 15 digital counts, which was typically less than one percent of the maximum intensity of the jet, and was deemed to be negligible. The calibration was completed before each set of daily experiments to remove the effects of temperature and pH, and provide accurate calibration curves for each experiment.

The calibration curves were used to process the experimental data. First, the series of experimental images was averaged to remove the flow fluctuations from the images. The background concentration was then removed from experimental images, leaving only the fluorescent intensity in the images. After the background intensity was removed, the calibration curves for each pixel were used to translate each pixel value into a concentration which was independent of the non-uniformity of the laser sheet. This concentration was used for the calculation of either the aspect ratio and perimeter of the elliptical cross section or the trajectory of the jet in the cross-flow.

2.4 Aspect Ratio Measurements

Measurements of the jet traveling vertically after its impingement on the step were taken to determine its shape and size. Preliminary investigations showed that time averaged images of the jet at this location resembled an elliptic jet. Elliptic jets are typically categorized in terms of their aspect ratio [21, 45]. As such, experiments were undertaken to determine the aspect ratio, perimeter and area of the jet exiting the crater. From this, a scaling factor and entrainment model based on the shape of the jet entering the cross-flow could be created to predict the trajectory of the plume. Measurements were taken using the PLIF system outlined in Section 2.3. The laser sheet was positioned parallel to the floor of the water channel, with its center approximately 2 mm above the top of the step. The orientation of the laser sheet with respect to the test section is shown in Figure 2.5. These measurements showed the cross section of the jet showing the jet width (parallel to the step) and depth (parallel to the mean velocity vector of the cross-flow). An isometric view of the impinging jet traveling through the measurement plane is shown in Figure 2.7. The camera used in these measurements had a spatial resolution of 0.25 mm per pixel. It should be noted that the laser sheet is approximately 4 pixels thick, which decreases the overall resolution of the measurements. Time averaged images of the jet were taken using 500 images with an exposure time of 10 ms and a frame rate of 7.6 FPS, producing the average jet concentration profiles over an approximate time period of 66 seconds.

Figure 2.8 shows the elliptical approximation of the jet's shape compared to the measured jet. Despite some skew and noise in the data, the ellipse provides a reasonable representation of both the shape and size of the deflected jet. The ellipse was defined based on its aspect ratio and perimeter. The jet aspect ratio (S) was defined as the ratio of the maximum jet width to the maximum jet depth at a concentration equal to 70 percent of the maximum jet concentration in the measurement plane. This 70 percent contour was determined based on experimental results. It was found that the 70 percent contour gave the best representation of the shape of the vertical jet entering the cross flow, encompassing the greatest portion of the jet and neglecting the noise in the measurement caused by the re-entrainment and spread of the jet fluid from further downstream. The maximum concentration was determined by finding the average of the 30 pixels with the highest concentration. This was used to minimize the effect of any wild data points caused by reflections or other noise in the image. To find the jet width and depth, a gaussian fit was used along each row and column of the average concentration matrix. The gaussian fits were produced by taking the logarithmic value of each point and fitting a parabola through each row and column. The parabolas were then converted back to normal space by taking the exponential of each function. The quadratic equation was then used to find the two points of intersection between the 70 percent concentration and the fit lines, and the difference between these two roots was determined to give width or depth. The jet aspect ratio was then found by dividing the maximum width (a) by the maximum depth (b) as shown in Equation 2.2. The perimeter of the ellipse was approximated using Equation 2.3 [46].

$$S = \frac{a}{b} \tag{2.2}$$

$$P = \pi \left[2(a^2 + b^2) - \frac{(a-b)^2}{2} \right]^{1/2} \tag{2.3}$$

2.5 Jet Trajectory Measurements

Jet trajectories were measured using the PLIF system with the laser sheet aligned parallel to the jet and cross-flow and perpendicular to the floor of the water channel as shown in Figure 2.6. Measurements were taken from the impingement point to approximately 8 d downstream of the step. Images were taken with exposure times of 10 ms, with a frame rate of 13.6 frames per second. Here the exposure time is longer than the time taken for fluid to travel through a pixel. This leads to some averaging within each instantaneous image. Because of this blurring, only averaged images were used in the analysis of the images. The averaged images used 500 single images, yielding a measurement time of 36.8 seconds. The spatial resolution of the camera was 0.27 mm/pixel. The jet trajectory was defined as the location of the maximum scalar concentration which was determined by finding the maximum concentration in each vertical column of the average concentration matrix. Power law curves were fit to the maximum scalar data to represent the jet trajectory.

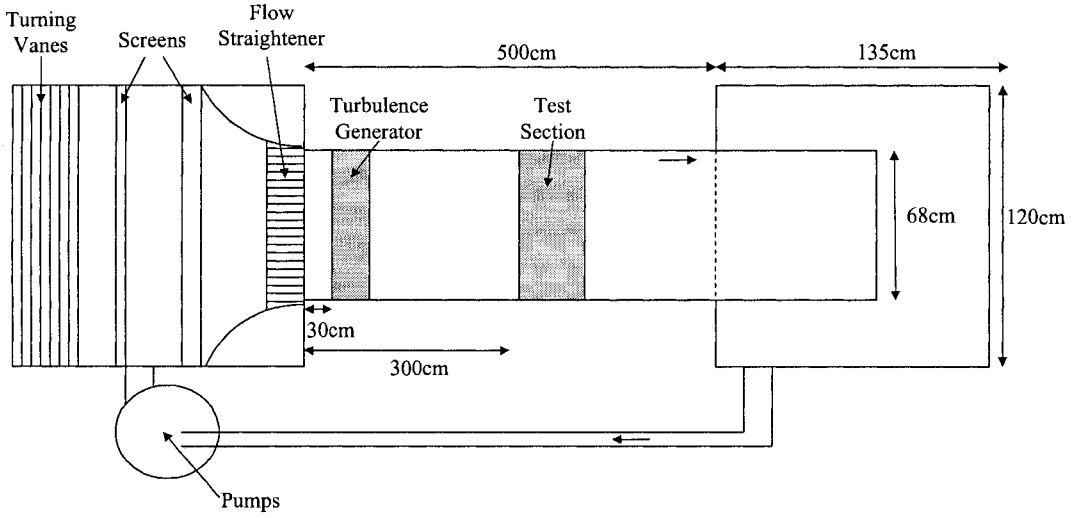

Figure 2.1: Schematic of the water channel. Details of the turbulence generator and the test section are shown in Figures 2.2 and 2.3 respectively.

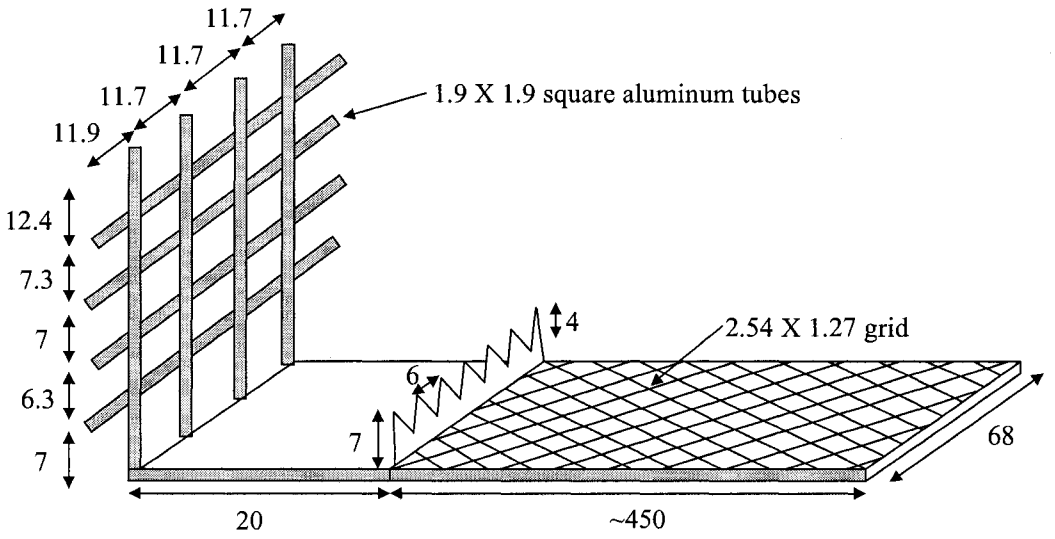

Figure 2.2: Schematic of the turbulence generator located at the inlet of the water channel. The water channel setting is the same as that used by Hilderman [43]. All dimensions are given in cm.

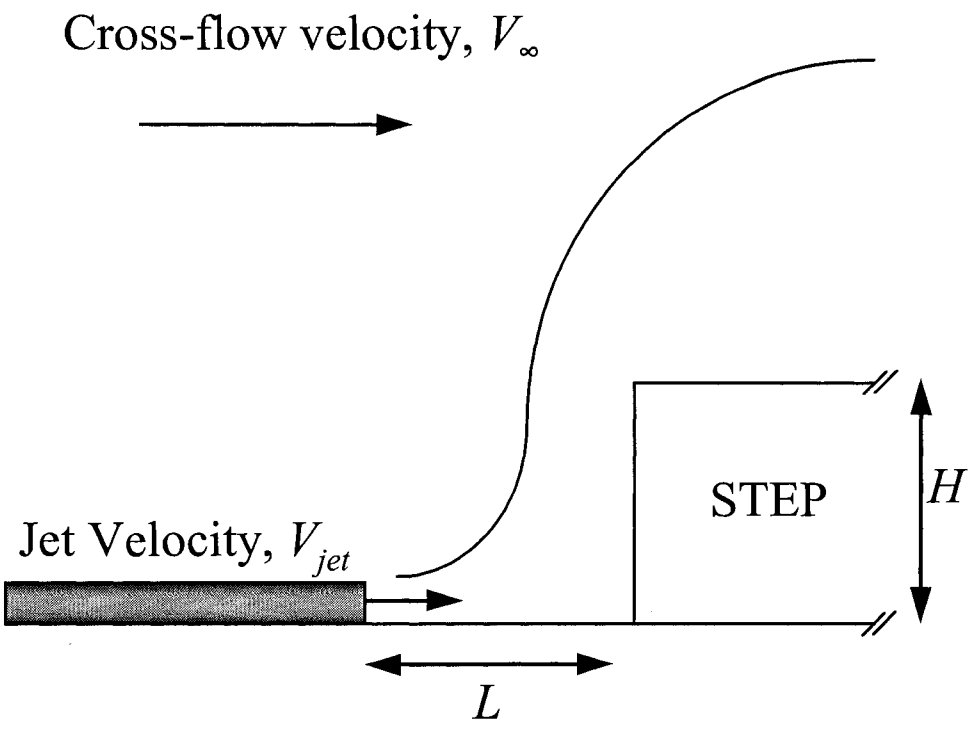

Figure 2.3: Schematic of the test section, located 3 m from the inlet of the water channel. Dimensions which are designated with a letter (H, L, V_{jet}, and V_∞) were varied for the parametric study.

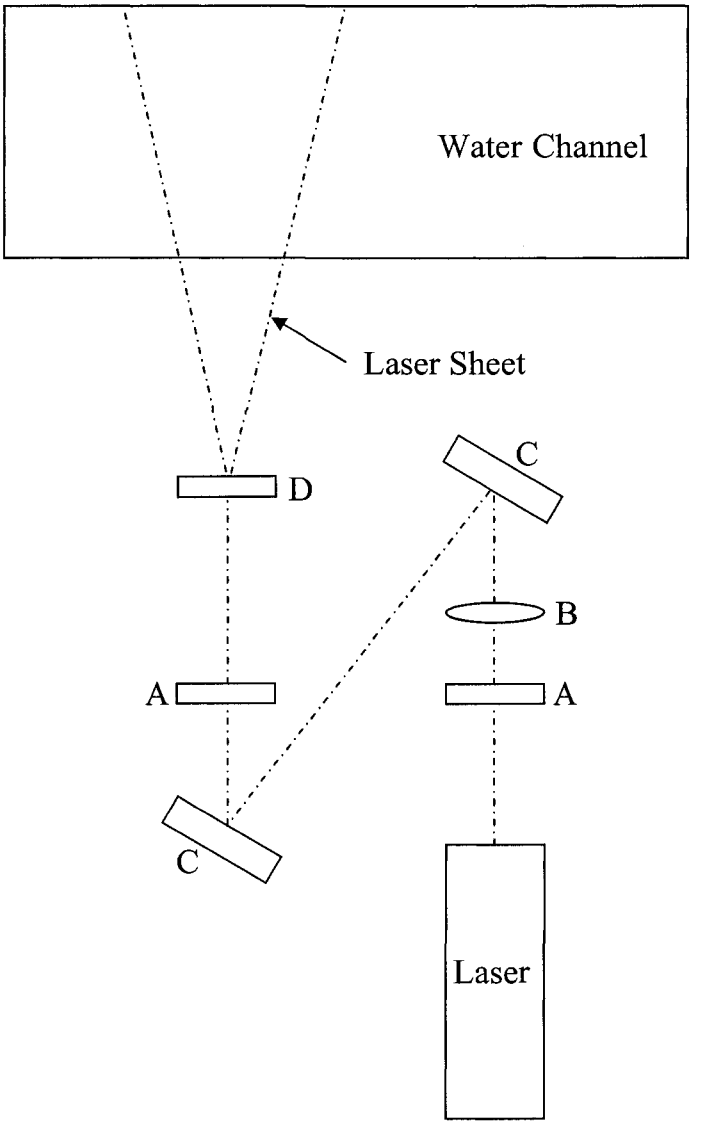

Figure 2.4: Laser sheet optics schematic. The diagram shows two apertures (A) used to minimize back reflection, a focusing lens with a 1 m focal length (B), and two steering mirrors (C) used to direct the beam onto the 30° divergence Powell lens (D). The beam path is shown by the dashed line.

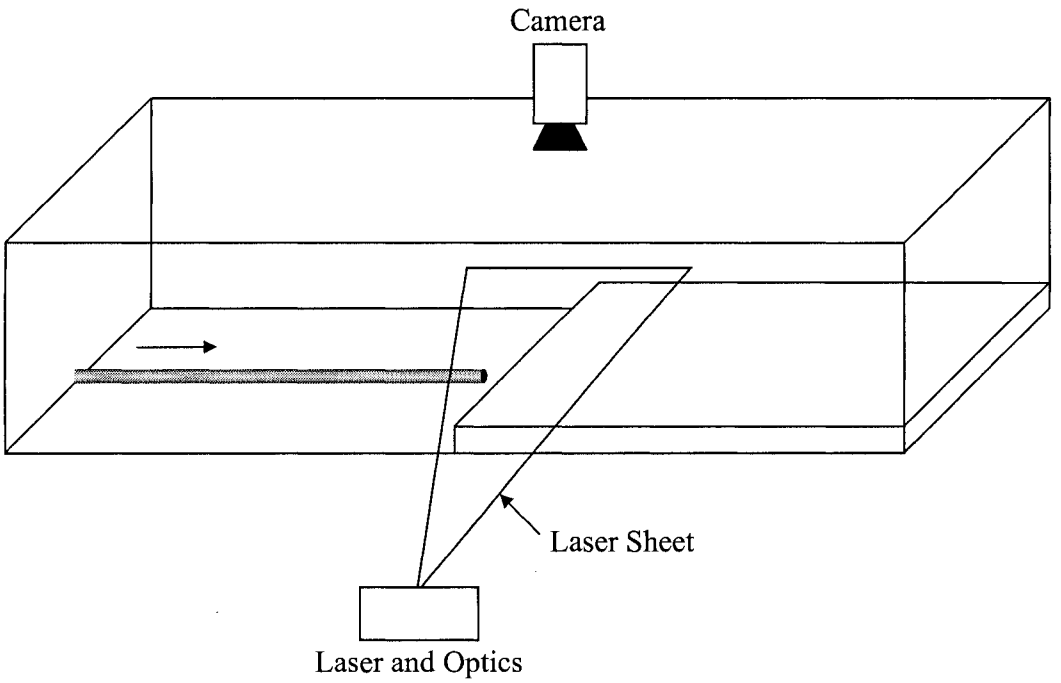

Figure 2.5: Laser sheet orientation and water channel schematic for aspect ratio measurements. The laser and optics are shown in detail in Figure 2.4.

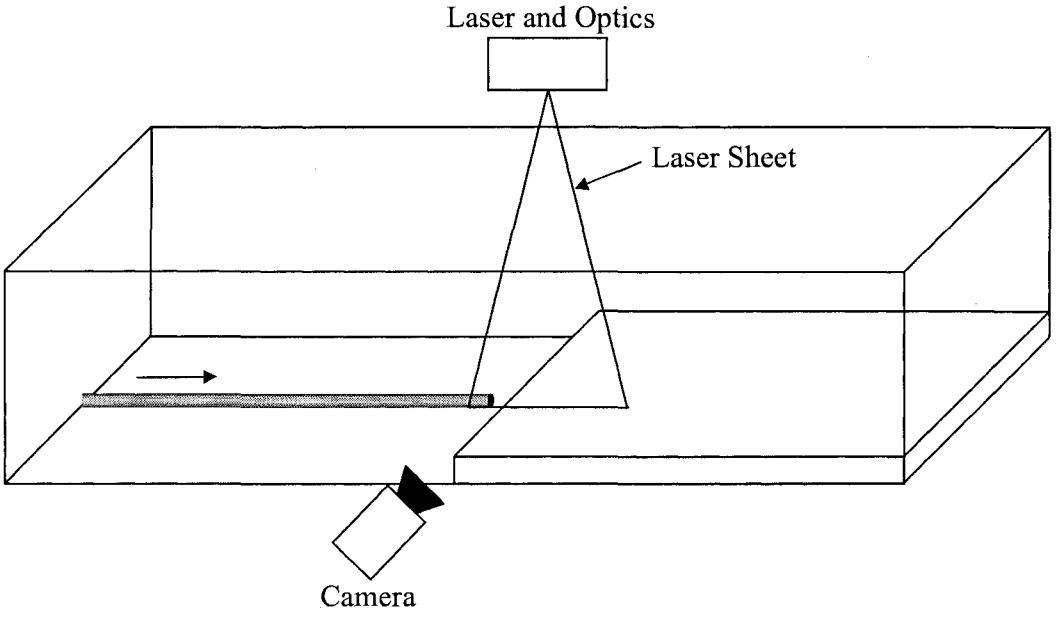

Figure 2.6: Laser sheet orientation and water channel schematic for jet trajectory measurements. The laser and optics are shown in detail in Figure 2.4.

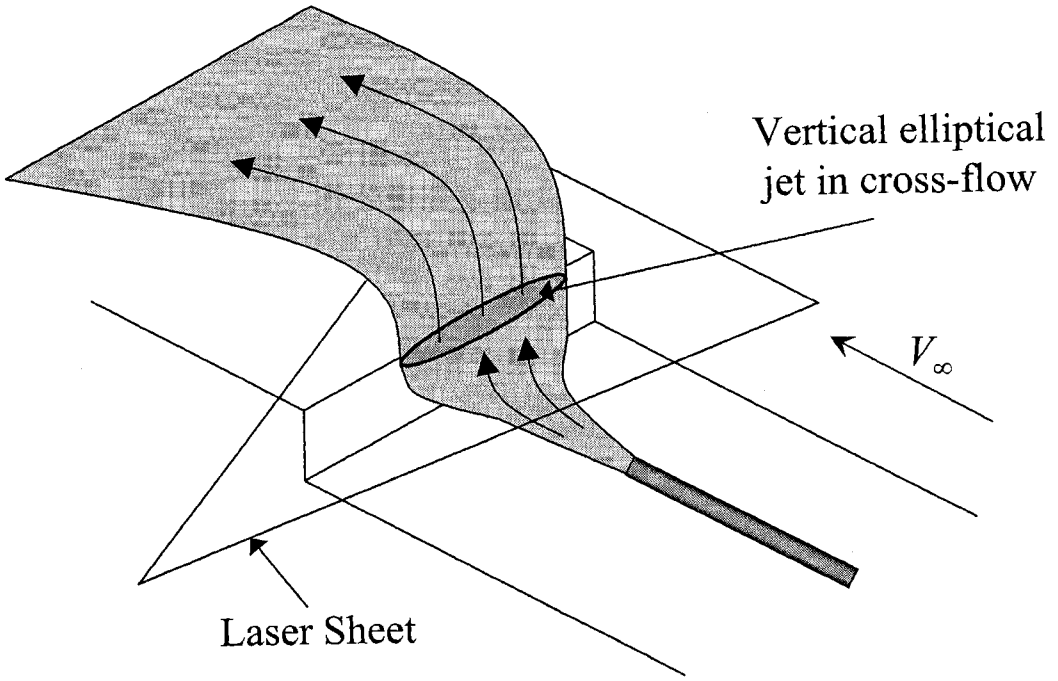

Figure 2.7: Isometric view of the jet impingement. Shaded area shows the measured elliptical cross section of the vertical jet entering into the cross-flow.

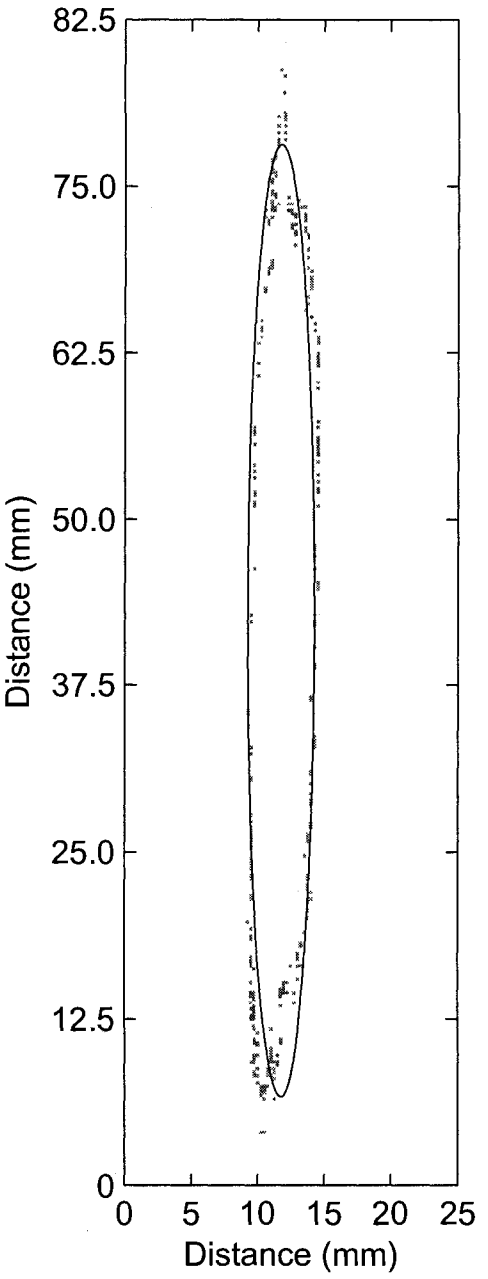

Figure 2.8: Example fit of the elliptical cross-section to an average image. The solid line shows the fitted ellipse, and the points outline the locations with 70 percent of the maximum concentration.

Chapter 3

Crater Region

3.1 Introduction

This chapter examines the effect of the jet-step interaction on the behaviour of the jet issuing vertically into the cross-flow. This interaction was studied by analyzing the shape and size of the elliptical jet measured in the plane parallel to the top of the step (location b in Figure 3.1). A combination of CFD simulations and PLIF measurements were used for this analysis.

CFD simulations were undertaken to determine the feasibility of using numerical methods to predict the behavior of the flow. The CFD simulations were modeled using ANSYS-CFX which solves the RANS equations using a standard k-ϵ turbulence closure model. The k-ϵ model has been used by several researchers to simulate the flow of free jets [36] and impinging jets [47]. If these methods are deemed feasible for predicting the flow, more advanced turbulence models could be used to produce more accurate models for further

parametric studies.

PLIF measurements were used for both flow visualization of the structures in this region and to measure the concentration profiles within the jet. Preliminary experiments showed that the jet exiting the step was elliptical in nature and the aspect ratio was dependent on the jet velocity (V_{jet}), cross-flow velocity (V_∞), step height (H), and the distance from the jet to the step (L). This study aims to determine how these parameters influence the shape and behavior of the jet as it is deflected into the cross-flow. The combination of experimental and CFD results provides insight into the jet-step interactions in this novel geometry under several different flow conditions.

3.2 CFD Constraints

3.2.1 Geometry

The geometry used for the simulations was identical to that used in the water channel experiments. The cross-flow was allowed to develop for one meter before and after the step to minimize the effects of the inlet and outlet conditions. A symmetry argument along the center of the channel was used to decrease the computational effort and time required for each test. This argument was justified by the centerline symmetry present in: the wall jet, the impinging jet, and the jet in cross-flow. The depth of the channel in the model was identical to that of the experimental system to best mimic both the cross-flow boundary layer and the penetration of the jet into the cross-flow. A dimensioned diagram of the

model is shown in Figure 3.2. The two dimensions which are given by letters (L and H) were varied in different simulations. The length, L, was set at 5, 10, and 15 d (43.75, 87.5, and 131.25 mm), and the height, H, was set at 25.4, 38.1, and 50.8 mm.

Boundary Conditions

The locations of the boundary conditions are shown in Figure 3.3. The inlet condition for the cross-flow had three initial normal speeds: 0.041, 0.061, and 0.081 m/s, all with an initial turbulence intensity of 1 percent. This level of turbulence intensity was due to the low Reynolds number and the effect of the turbulence generator upstream, and matched the experiments. The inlet was defined as a subsonic flow with a scalar concentration of 0 mg/L. The jet inlet was also a subsonic flow, with an initial concentration of 0.7 kg/m^3. The jet velocity was set at three different normal speeds: 0.47, 0.78, and 1.10 m/s, with a turbulence intensity of 5 percent. An average static pressure condition was used at the outlet, which was set at zero pascals relative to the flow. The bottom of the channel, the step, and the side wall were all set as smooth walls with the no-slip condition. Due to the increased computational cost, the effect of roughness on the walls was not included. The top of the channel was set as a wall with free slip to best simulate the free surface at the top of the experimental water channel.

Meshing

Three computational grids were used to determine the effect of grid dependence; the grids were designated as coarse, medium, and fine. The grid used for all of the simulations (except the grid convergence study) is shown in Figure 3.4. Due to computer limitations the coarse grid was used for the parametric study, and only one simulation was run using each the medium and fine grids. Since the purpose of the CFD study was to determine the feasibility of using computer simulations to predict the perimeter of the jet, the usage of the coarse grid was justified. The parametric study required several different simulations (and significantly more computational effort), further justifying the use of the coarse grid. An analysis of the effects of using the coarse grid on the accuracy due to grid dependence is discussed in Section 3.2.1.

The three grids used had spacings of 2.5, 2, and 1.5 cm between nodes in the free stream region. Along the floor of the channel and on the step, inflation was used to increase the number of elements near to the walls. In all cases, the inflated layer had a maximum thickness of 10 cm and the expansion factors used were: 1.1 for the coarse and medium grids, and 1.08 for the fine grid. There were 15 inflated layers in the coarse grid, 20 in the medium, and 30 in the fine grid. Each grid also had a region of refinement around the step, as this was the region with the largest flow gradient and was also the area of greatest interest. Two cylindrical regions located along the two corners of the step with a radius of 8 cm were used for grid refinement. In these regions the spacing between nodes was 0.8, 0.6, and 0.5 cm respectively for the coarse, medium and fine grids. The expansion factor in these

regions was 1.1 for the coarse and medium grids, and 1.07 for the fine grid. With these characteristics, the number of nodes for each grid were 99646, 198341, and 397942. This lead to a grid refinement factor, r, of 2.0.

Solver Parameters

The software used a 'coupled multi-grid solver' to solve the linear system of discretized equations. The advection scheme selected in the CFX software was the 'high resolution advection scheme'. CFX defines a blending factor which will be referred to as ϕ (but is β in the CFX manual), which represents the order of the numerical scheme, with $\phi = 0$ representing an upwind differencing scheme, and $\phi = 1$ representing a second-order accurate scheme. The high resolution advection scheme sets ϕ as close to 1 as possible without introducing oscillations into the flow. This resulted in ϕ being variable throughout the flow, with a solution which was greater than first order accurate (though not fully second order) throughout the domain. Values of ϕ for a line along the jet centerline for the vertical velocity component is shown as an example in Figure 3.5.

The standard k-ϵ model with a scalable wall function was used for the turbulence within the flow. The coefficients for this model were: $C_\mu = 0.09$, $C_{\epsilon 1} = 1.44$, $C_{\epsilon 2} = 1.92$, $\sigma_k = 1.0$, and $\sigma_\epsilon = 1.3$. The scalable wall function [48] limits the value of y^* (to be greater than 11.06) to avoid placing mesh points within the viscous sub-layer (which produces the inconsistencies outlined by Grotjans [49]). Although the k-ϵ method has been shown to over-predict turbulent spreading in round jets and can "fail profoundly" for three-

dimensional flows [33], it provided fast convergence and was sufficiently robust for all of the flow conditions. Other methods such as the shear stress transport model, and two Reynolds stress models (BSL and SSG), were tested but produced oscillatory results for the conditions used and would not converge. Using a different solution scheme or further grid refinement may have improved the convergence of these methods.

A stationary solution was found for the simulation in order to minimize its computational cost. Since the experiments were performed to determine averaged concentration intensities, a steady state approximation was all that was required. The timescale and length scale used in the solution used the default settings: automatic and conservative respectively. The required convergence level was set to an average residual of 10^{-6}. The effect of the residual on the jet perimeter is shown in Table 3.1 which shows that the choice of residual causes less than a one percent variation in the perimeter. The passive scalar transport equation was used to determine the movement of the scalar throughout the flow. The remainder of the tuning parameters present in the software remained at their default settings.

Grid Independence and Uncertainty

The uncertainty in the results produced by this simulation was determined primarily through the methods outlined by Roache [39]. The validation method defines a grid convergence index (GCI) which is given in Equation 3.1. The GCI is meant to be used as both an estimate of the error bars which surround the simulation data, and a method of reporting grid convergence. The error is approximated for the coarse grid by using the fine grid as a

reference [39].

$$GCI_2^{coarse} = F_s|E_2| \tag{3.1}$$

Where: F_s is a safety factor, for which a value of 3.0 is recommended for conservative estimates of the errors [39], and E_2 is defined in Equation 3.2.

$$E_2^{coarse} = \frac{r^p \varepsilon}{1 - r^p} \tag{3.2}$$

Where: $\varepsilon = f_2$ - f_1, gives the variation in the parameter of interest (perimeter in this case) between the coarser grid (2) and the finer grid (1), r is the refinement factor, which is the ratio between the size of the control volumes between the coarse and fine case, and p is the formal order of accuracy of the algorithm, which is defined in Equation 3.3.

The order of accuracy of the simulation algorithm (p) can be calculated through the use of a three grid refinement study, providing the grid refinement ratio is constant [50]. The equation defining the order [50] was used in the formulation of the GCI, so Roache's [39] notation is used, shown in Equation 3.3. In this study, the parameter of interest is the perimeter of the vertical jet issuing from the step, denoted by f in the general form [39].

$$p = \ln\left(\frac{f_3 - f_2}{f_2 - f_1}\right) / \ln(r) \tag{3.3}$$

Where: f is the parameter of interest in the three grids being tested, with the subscripts 1, 2, and 3 representing the finest, medium, and coarsest grids studied.

The uncertainty of the measurements from this model was determined based on the order and GCI. The order, p was found to be 1.2. From this, the coarse GCI (relating the medium grid to the coarse grid) was calculated for the jet's perimeter and found to have a value of 28 mm, representing the approximate error bars for the system (due to the discretization error). If more computing resources were available, the fine grid could be used, which had a GCI (when compared to the medium grid) of 12 mm.

To ensure that the grid has reached its asymptotic convergence rate, Roache [39] recommends using Equation 3.4 (modified from using the finest grid to the coarsest grid). If γ is equal to r^p, then p is in fact the order of the convergence (the method is p-order accurate), and lies within the asymptotic range of convergence. For this study, γ was found to be 2.31, and r^p was found to be 2.30. This is a difference of 0.01 or a percent difference of 0.6, and $r^p \approx \gamma$. Thus, this study is 1.2 order accurate, and all of the grids are within the asymptotic range.

$$\gamma = GCI_{12}^{coarse}/GCI_{23}^{coarse} \tag{3.4}$$

Truncation errors for low order systems (like this simulation) have been shown to cause significant effects on the modeled flow behavior [51]. When solving the RANS equations, the computer uses truncated Taylor series to represent different functions. In the case of a first order solver, the second order terms are truncated. Since viscosity is a second order term in the RANS equations, the truncated terms are absorbed into the viscosity term. This causes the modeled viscosity to be larger than the actual viscosity, leading to artificial

diffusion in the flow. Because of this, it would be expected that this model will over-predict the spreading rate of the jet.

The third primary source of uncertainty in this study is caused by the assumptions implicit in the k-ϵ model. The k-ϵ model, though commonly used in flow studies, was designed primarily for two dimensional shear flow problems. The model assumes that "zero velocity gradient is accompanied by zero shear stress" [52]. In cases with large streamline curvatures and large pressure gradients, such as impinging jets, the k-ϵ model can be inaccurate [33]. Cusworth [36] found that the k-ϵ model over-predicted the turbulent kinetic energy (on the order of 30 percent), and thus the spreading rate of a free round jet. The model can also highly over-predict the rate of heat (or scalar) transfer within flows [47]. From this, it can be assumed that the use of the k-ϵ model will lead to over-prediction of diffusion and the spreading of the jet in the study presented here. Modifications of the coefficient in the eddy viscosity C_μ term can minimize this over prediction [34], and could be used later to improve the accuracy of this model. As the purpose of this study was to determine the feasibility of using CFD and not to model the flow exactly, these coefficients were not modified.

There are large uncertainties in the solution method used for this study due to modeling, truncation, and discretization errors and as such, it should be expected that the CFD results over-predict the spreading rate of the jet. This simulation is, however, computationally inexpensive, and predictions of the trends in the jet perimeter for parametric studies could be very valuable. Further improvements on the computational model could be made to improve the predictions of the jet perimeter in the future if it is deemed feasible based

on the results of this study.

3.2.2 Perimeter Measurement Method

The perimeter and aspect ratio of the ellipse encircling the 70 percent of the maximum concentration contour lines of the flow were determined from the CFD models. The measurements were made by analyzing the contour lines along a horizontal plane located at the top of the step ($z = 0$mm). Contours on this plane are shown in Figure 3.14 (parts c and d) for a standard case. The 70 percent contour was isolated and measured to determine the width and depth of the contour using the tools available in CFX. From this, the perimeter and aspect ratio were calculated in the same manner as the experimental results.

3.3 PLIF Results

Experiments to determine the effects of three parameters: L, H, and R (shown in Figure 3.1 were used in this study. An example of instantaneous jet measurements is shown in Figure 3.6 which shows the structures present in the flow. The measurements of the jet depth and width were based on Gaussian curve fits along each row and column of the average images. The fits for the depth and width are shown in Figures 3.7 and 3.8 respectively.

The values of L, H and R were varied for the parametric study. For each case, the average of all of the tests taken at each flow condition (typically two runs) was used to determine the perimeter and aspect ratio, and the uncertainty was approximated by taking

two times the standard deviation of one condition where five independent tests were performed. Figure 3.9 shows that the relation between perimeter and length is nearly linear for all of the step heights. Figure 3.10 shows the effect of the step height which also possesses linearity. From these figures it is apparent that the step height has a slightly stronger effect on the jet's perimeter than the distance from the jet to the step. The slope of the two curves varies by a factor of approximately 4. For simplicity, this difference was neglected in forming the correlations for the perimeter. It should also be noted that a 1/2 power law fit would also fit the data within the error bars, and further data points would be required to determine the exact relationship between the perimeter and the step height and distance from the step. Figure 3.11 shows the perimeter compared with the logarithm of the velocity ratio for a constant step height ($H = 38.1$ mm) and a constant length ($L = 9\ d$). This data was used to create the universal scaling laws which are proposed in the next section.

3.4 Discussion

3.4.1 Empirical Perimeter Correlation

An empirical correlation predicting the perimeter of the jet based on R, L and H was determined using the data presented above. In order to better fit the model, the length L was altered to the distance from the origin of a point momentum source to the step (L_o). Based on the jet's spreading rate its approximate location was assumed as 5 diameters behind the jet outlet. This produced the empirical correlation given in Equation 3.5, and shown in Figure 3.12. From the fit, it can be seen that this model predicts the perimeter within a

13 percent error for all of the data points. This correlation provides a model which predicts the perimeter of the jet entering the cross-flow for all of the H, L_o, and R values tested.

$$\frac{P}{d} = 1.84\ R^{\,0.2} \left(\frac{HL_o}{d^2}\right)^{1/2} - 5.79 \tag{3.5}$$

It should be noted that in developing this relationship, several different relations of the perimeter with H and L were tested. Logically, it would be expected that the perimeter would increase with the total distance traveled along the wall, such that the perimeter would be related to $(H + L_o)$ or $(H^2 + L_o^2)^{1/2}$. These relationships were tested and it was found that the best correlation occurred when the product of H and L was used as shown in equation 3.5. The correlation for P (Equation 3.5 shows that the curve fits for Figures 3.9 and 3.10 could be represented by 1/2 power law fits. These figures were shown with linear fits to help demonstrate the trends in the data.

Both Equation 3.5 and Figure 3.12 normalize the perimeter by the inlet jet diameter. This scaling is not fully justified by the experiments, as only one diameter was tested. The diameter is a convenient factor which is used frequently in the literature for non-dimensionalizing the length units of jets. Further experiments are required to fully justify this scaling. Attempts at finding a different length scale to produce non-dimensional groups were unsuccessful. However, it is possible that a turbulence or friction length scale could be used instead of the jet diameter.

3.4.2 Experimental Aspect Ratio Correlation

To fully define the shape of the ellipse representing the vertical jet entering the cross-flow, the perimeter and aspect ratio (S) are required. The experimental correlation for S related to the inlet conditions is given in Equation 3.6 and shown in Figure 3.13. In this correlation it is apparent that the ratio of H and L_o is used instead of their product (as used in Equation 3.5). As L_o increases, the wall jet grows vertically, which, upon impingement, leads to an increase in the ellipse's depth. It was found that the rate of growth of the depth is significantly larger with L_o than H when compared to the growth of the width. This leads to a decrease in S with increasing L_o. Figure 3.13 shows greater variability in the data at higher aspect ratios, which is most likely due to the uncertainty in the depth measurements.

$$S = 8.38 \left(\frac{H}{L_o} \right)^{0.3} R^{0.4} \tag{3.6}$$

3.4.3 Comparison of CFD to Experimental Data

A comparison of the concentration profiles along the measurement plane is shown in Figure 3.14. Parts (a) and (c) show the concentration profile on a linear scale which appears to have similar shapes for both the actual and modeled jets. Parts (b) and (d) used a saw-tooth concentration profile which emphasized the structures in the flow. From this, it can be seen that the simulation accurately predicted the elliptical shape of the vertical jet, though with slightly larger depth than the experimental case. The location of the counter-rotating

vortex pair downstream of the jet was also accurately predicted by the simulation. The comparison of the flow visualization images shows that the CFD code can clearly predict the mean characteristics of this flow.

The perimeters of the ellipses formed by the 70 percent contours for all of the experiments and simulations are shown in Figure 3.15. It can be seen that the perimeters predicted by the simulation do not match those determined experimentally within their uncertainty. They do however predict a similar trend and could be used to provide an approximation for the perimeter based on the inlet conditions. The error bars for the CFD measurements shown in the figure are those recommended by Roache [39] and are equal to the GCI outlined in Equation 3.1. Despite the prediction of the trend, the error bars are significant and it should be noted that a horizontal line with a value of approximately $P/d = 25$ can be drawn through the error bars. A comparison of the aspect ratios is shown in Figure 3.16 which shows significant overlap between the CFD and experimental results. From this, it can be seen that the shape of the ellipse (shown by its aspect ratio) is well predicted by the CFD model. This shows that the artificial diffusion discussed earlier effects the jet in all directions and leads only to an over-prediction of the size of the jet, while accurately predicting its shape.

Through comparing the CFD data to the experimental data, it can be seen that the CFD model can give a reasonable estimate of the actual value of the perimeter. The trend in the data is predicted to within 30 percent, with a constant over-prediction of about 50 percent. Despite this over-prediction of the perimeter, the model provides reasonable results

which could be used to perform further parametric studies on the effects of different flow conditions.

3.5 Conclusion

The study of the crater region has shown that the shape and size of the elliptical jet entering the cross-flow can be determined through empirical relationships. These relationships for the perimeter and aspect ratio of the jet were found to be dependent on H, L, and R and can be predicted with the relations given in Equations 3.5 and 3.6. These predictive models will be used as the initial conditions for the jet in cross-flow study presented in Chapter 4 which will predict the mean jet trajectory based on these initial conditions.

CFD measurements were found to accurately predict the structures within the flow and provide a reasonable estimate of the perimeter and aspect ratio of the jet. The trends of the parametric study predicted by the CFD model were found to follow those measured experimentally. This CFD model over-predicts the spreading of the jet, however, using a higher order solution method or a more accurate closure model could lead to more accurate predictions of the jet's size. Based on the accuracy of these simple models, further use of CFD models to predict this flow is recommended as they can be very useful for more detailed parametric studies. The CFD models could also be incorporated into more complete models for the crater released jet.

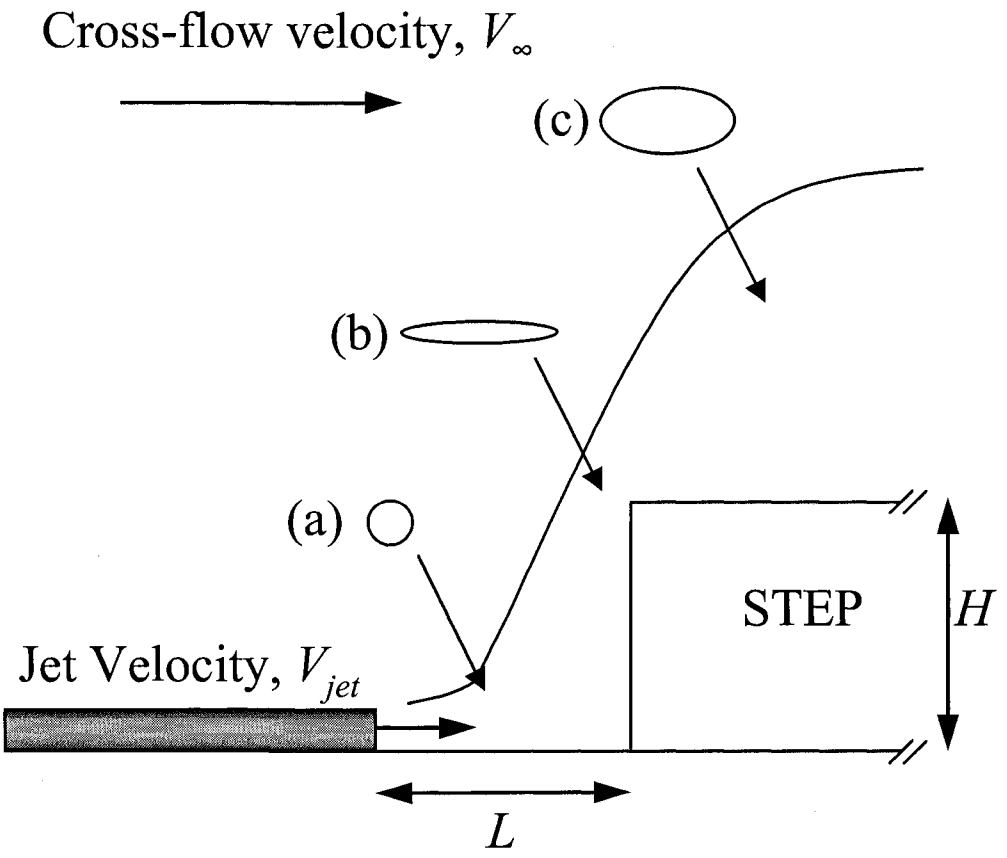

Figure 3.1: Schematic of the test section. The step height (H), the effective distance (L) and the velocity ratio ($R = V_{jet}/V_\infty$) were varied for the parametric study. The shape of the cross section perpendicular to the direction of the jet is shown at three locations: the pipe exit (a), the top of the step (b), and downstream of the step (c). The round jet flattens at the step (b) and forms a high aspect ratio ellipse which then grows primarily along its minor axis downstream.

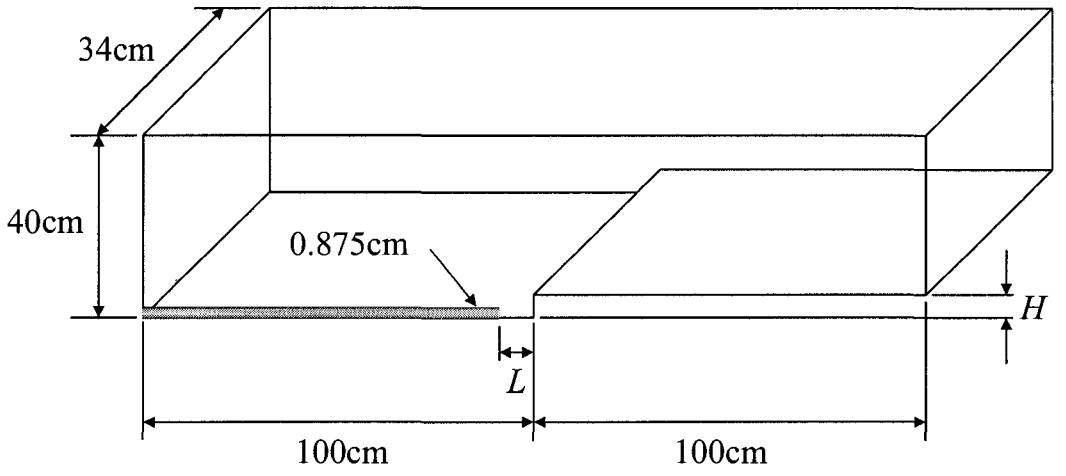

Figure 3.2: Dimensions of the model used for the CFD simulations. Dimensions were made to match the water channel facility.

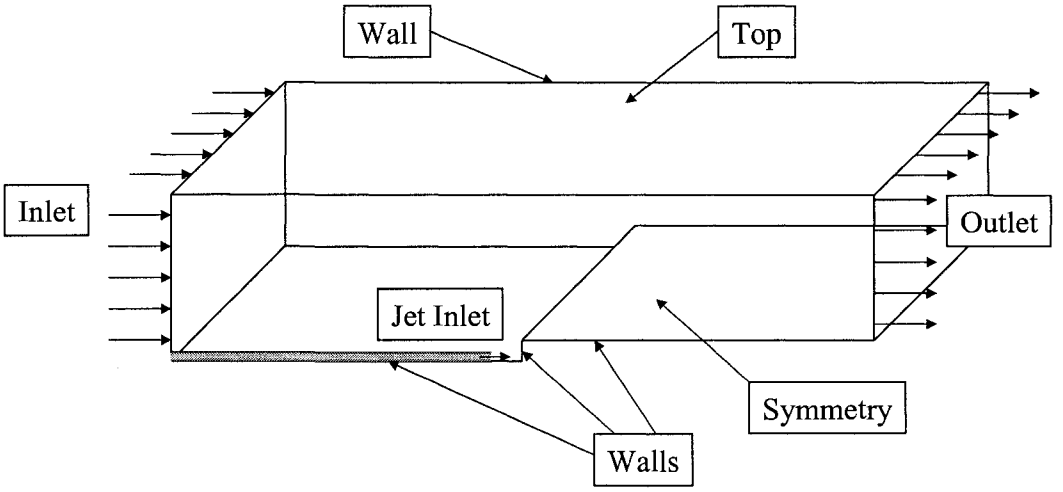

Figure 3.3: Types and locations of the boundary conditions used in the CFD model.

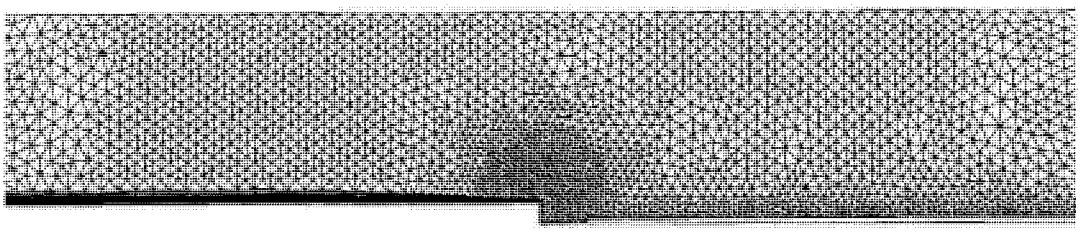

Figure 3.4: View of mesh through the symmetry plane for the coarse grid case. This is the mesh that was used for the simulations (with the exception of the grid refinement study).

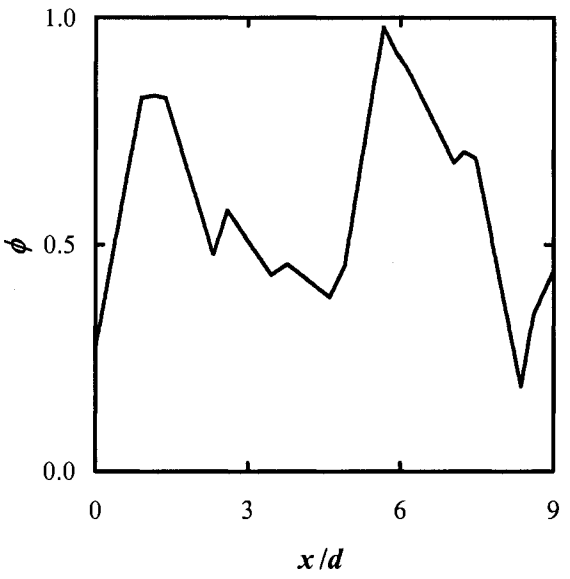

Figure 3.5: Variation in ϕ, the blending factor used in the CFD code where $\phi = 0$ represents a first order method and $\phi = 1$ represents a second order method. Values are for the vertical velocity along the major axis of the elliptical cross-section in the measurement plane. The global order of the solution was found to be 1.2, which corresponds to a ϕ value of approximately 0.2.

Table 3.1: Effect of the average maximum residual used for convergence on perimeter measurement. To save computational time, a residual of 10^{-6} was used for the simulations.

Residual	Perimeter (mm)
1.E-05	220.6
1.E-06	222.9
1.E-07	220.9
1.E-08	220.9

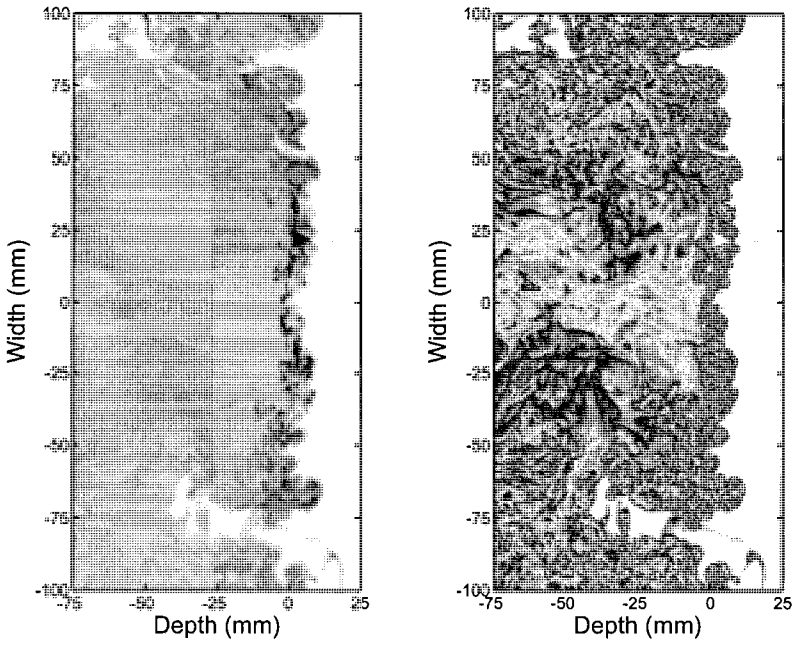

(a) (b)

Figure 3.6: Single experimental image of the concentration profile within the jet. A linear concentration scale is shown in (a) and a sawtooth scale used to emphasize the structures apparent in the jet is shown in (b). The cross-flow moves from right to left, with the jet fluid moving out of the page. The step is located at 0 mm.

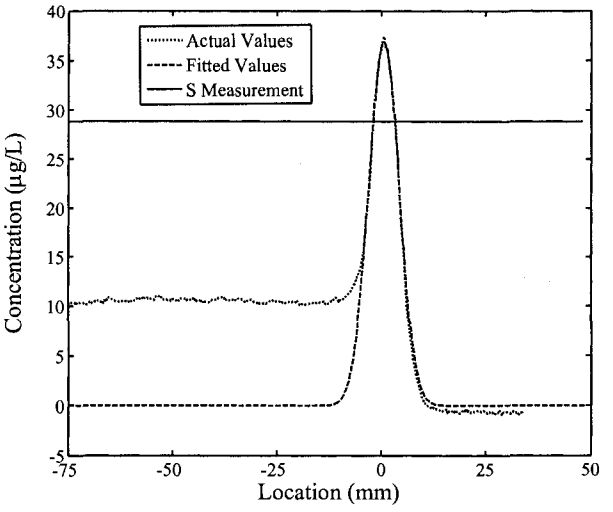

Figure 3.7: Measured concentration along the maximum depth line. The horizontal solid line shows the 70 percent value where the depth and width are measured. A threshold value of 60 percent of the maximum concentration was used to determine the Gaussian fit.

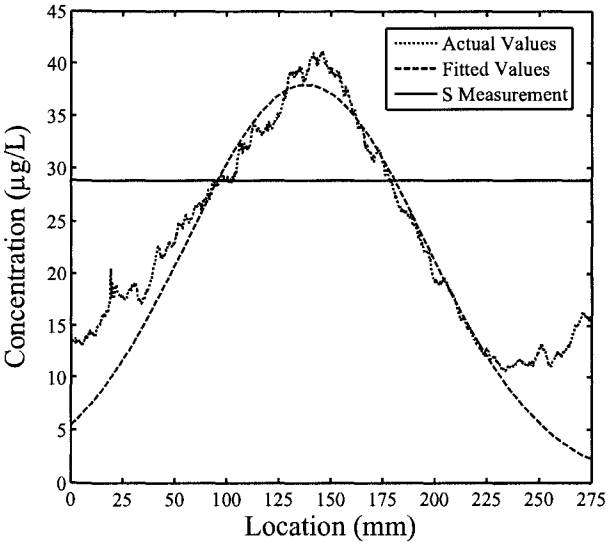

Figure 3.8: Measured concentration along the maximum width line. The horizontal solid line shows the 70 percent value where the depth and width are measured. A threshold value of 60 percent of the maximum concentration was used to determine the Gaussian fit.

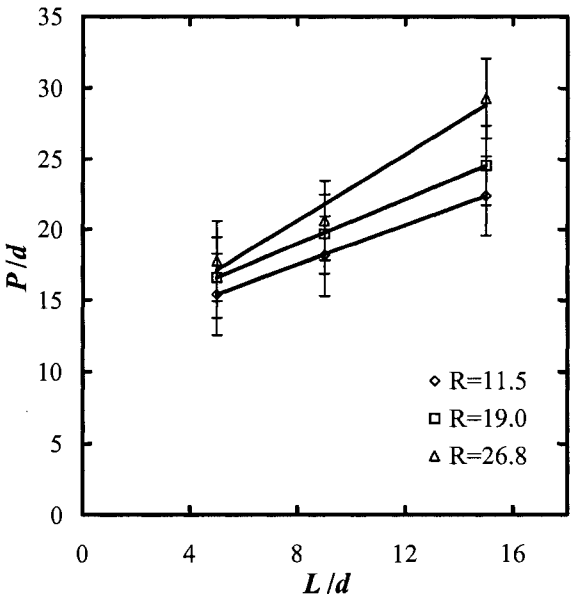

Figure 3.9: The effect of the step position (L) on perimeter using different velocity ratios and a constant step height. Normalized with the jet diameter d.

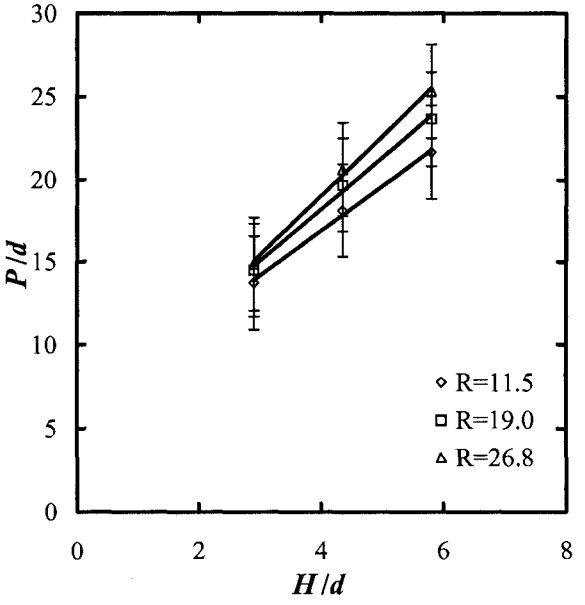

Figure 3.10: The effect of the step height (H) with different velocity ratios and a constant distance from the step. Normalized with the jet diameter d.

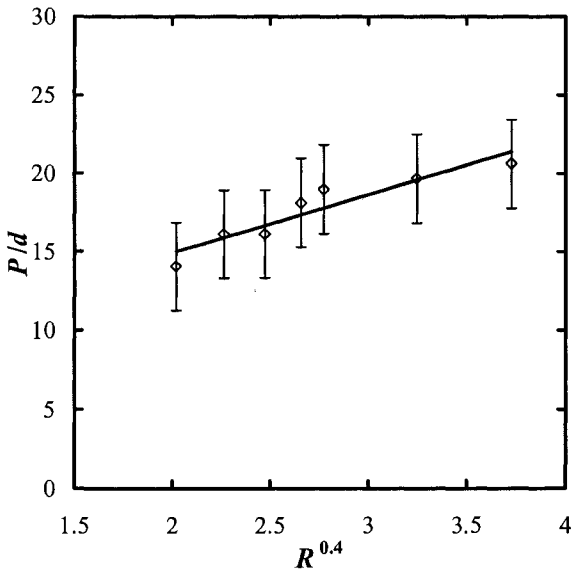

Figure 3.11: The effect of velocity ratio R for a single step height and distance from the step. Normalized with the jet diameter d.

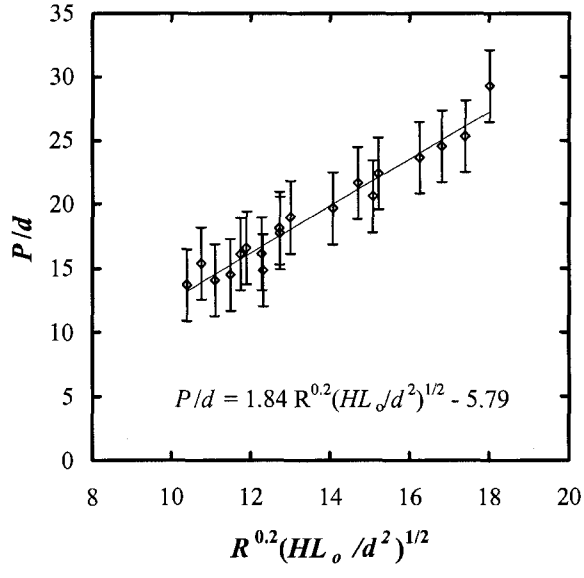

Figure 3.12: Measured perimeters compared with the experimental fit outlined in Equation 3.5. The error bars represent twice the standard deviation of the condition where 5 tests were taken.

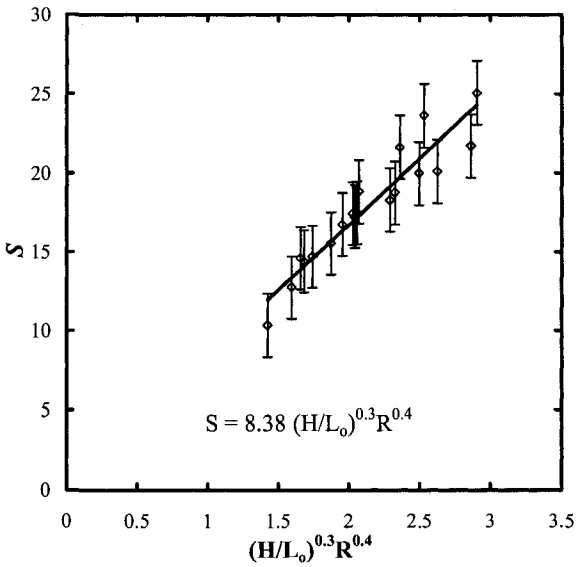

Figure 3.13: Experimental correlation for the jet aspect ratio S (defined in equation 3.6) based on the step height H, effective distance to the step $L_\circ$, and velocity ratio R.

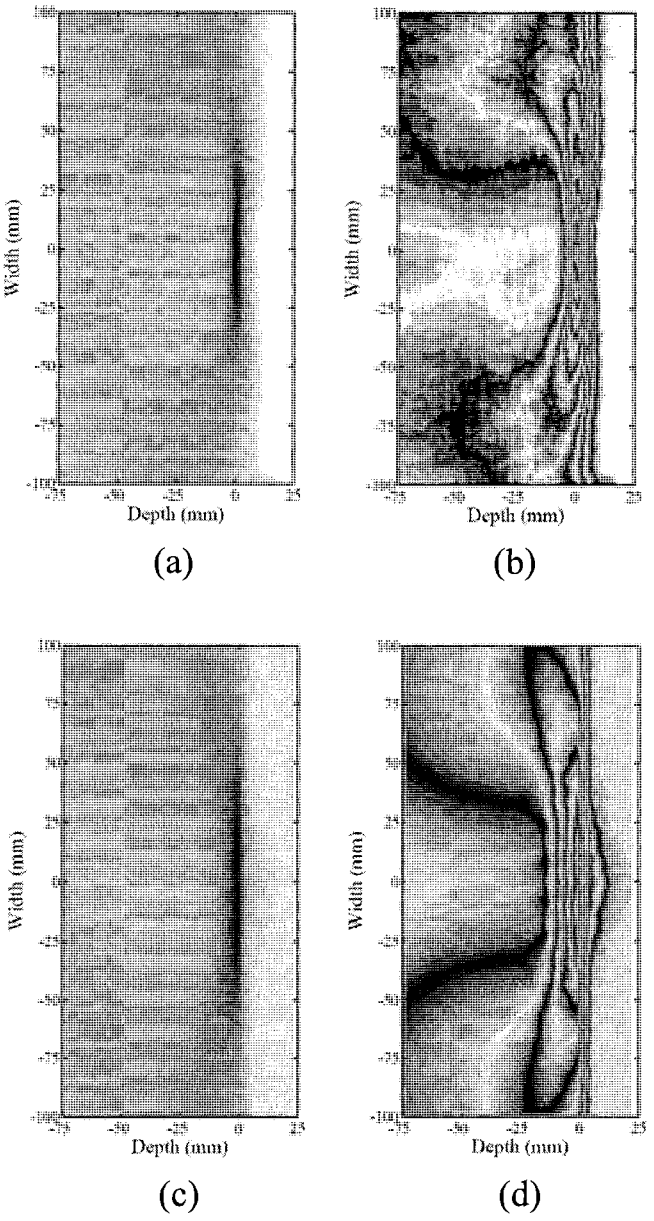

Figure 3.14: Experimental (a and b) and CFD (c and d) concentration profiles. Linear and sawtooth concentration scales are shown to emphasize flow structures. The cross-flow moves from right to left with the jet fluid moving out of the page. The step was located at 0 mm.

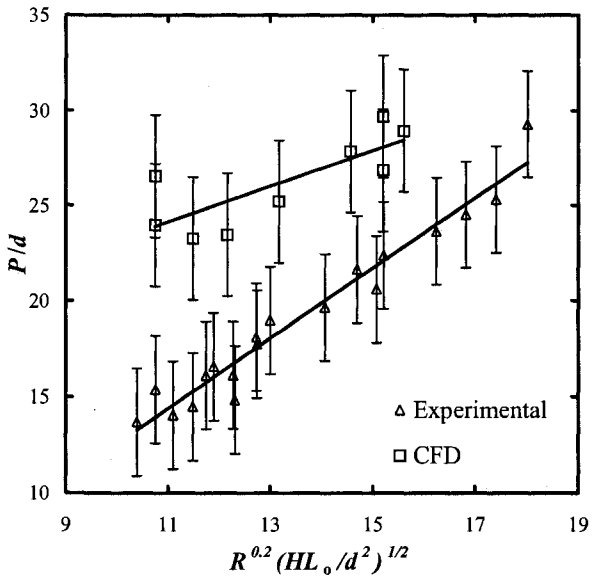

Figure 3.15: Comparison of CFD results to experimental results using the scaling relation given in Equation 3.5. CFD results slightly over-predict the perimeter due to the extra diffusion introduced into the flow caused by the use of the k-ϵ turbulence model and the order of the simulation. Error bars are based on the GCI as outlined by Roache [39] and calculated in Section 3.2.1.

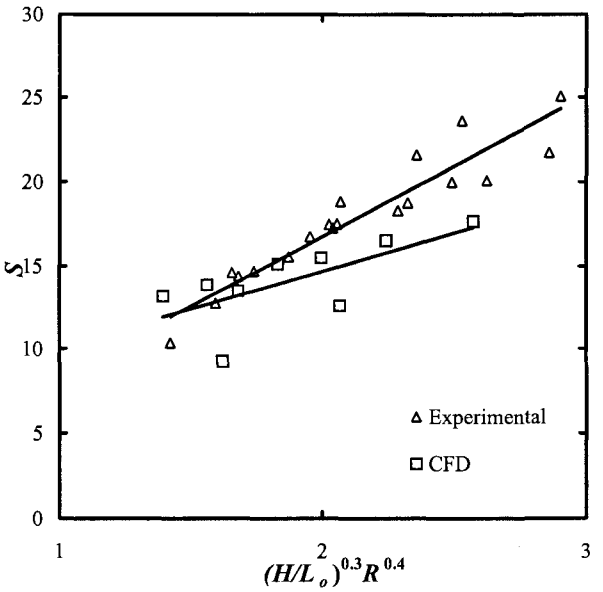

Figure 3.16: Comparison of aspect ratio measurements S for CFD results and experimental results in terms of the step height (H), effective distance to the step (L_o), and velocity ratio (R).

Chapter 4

Jet in Cross-Flow Region

4.1 Introduction

This chapter examines the trajectory of the elliptical jet as it enters the cross-flow. Jet trajectories were determined using PLIF measurements along the centerline of the jet. The jet trajectory was defined as the locus of maximum scalar concentrations measured along each vertical row of the average jet images. The results of Chapter 3 were used as initial conditions for this jet in cross-flow study. These initial conditions are given in the models for jet perimeter and aspect ratio given in Equations 3.5 and 3.6. In these equations, the geometric and velocity terms defining the flow are defined as: the step height (H), the effective distance from the origin of a point source to the step (L_o), and the ratio of the jet velocity to the cross-flow velocity (R). Given this information, the shape of the jet entering into the cross-flow is fully defined as a high aspect ratio ellipse, with a major axis perpendicular to the cross-flow, and a minor axis in the direction of the cross-flow velocity. This chapter will derive a predictive model of the jet centerline trajectory through the cross-flow

based on these parameters.

The round jet in cross-flow produced by an elevated stack has two distinct regions: the jet dominated region, and the bent-over plume region [19, 23]. In the jet dominated region, the trajectory can be modeled as a power law relating the height to the distance from the stack with an exponent of 1/2 [19]. After the jet has entrained sufficient cross-flowing fluid, the cross-flow momentum dominates, and in this fully bent-over region, a different power law relation with an exponent of 1/3 predicts the data [23]. The jet dominated region is very small, and only exists near the source [19]. In both cases, the jet to cross-flow velocity ratio has significant effects on the jet trajectory and was used to normalize the data (along with the stack diameter) and produce the power law relationships. For both round and elliptical jets, the flow is initially dominated by the jet's momentum, and as the jet entrains more cross-flowing fluid, the momentum of the cross-stream dominates the jet. The experimental data and predictions for the deflected jet will be compared with the analytical model presented by Briggs [23] to determine if a round-jet model can be used to predict the trajectory of the elliptical jet in cross-flow.

4.2 Empirical Correlations

This study examined the jet in cross-flow produced by a range of step heights, distances from the jet to the step, and velocity ratios. An example of an instantaneous measurement of the jet trajectory is shown in Figure 4.1. Figure 4.2 shows contours of an averaged ex-

perimental image. It was found that in all cases, the behavior of the plume could be scaled with the perimeter of the jet exiting the step. The use of P scaling showed three consistent regions in the vertical jet: the near-field, the mid-field, and the far-field regions. Examples of these fits for a single jet trajectory are shown in Figure 4.3.

All of the experiments showed that in the near-field region from $0 < x/P < 0.12$ the jet followed Equation 4.1. This is consistent with Weil who explains that in this region "the plume is dominated by its initial mass and momentum fluxes" [19]. Some examples of the curve fits for this region are shown in Figure 4.4. From this figure it can be seen that there is a strong correlation between the jet velocity ratio and the penetration of the jet into the cross-flow. The penetration is also affected by the geometric conditions of the impingement region (H and L) studied in Chapter 3. This is most likely due to the effects of these parameters on the jet's momentum. The spreading of the jet was found to increase with both H and L, causing increased surface area, and thus increased drag and entrainment. The effect of this momentum loss on Equation 4.1 is a decrease in the coefficient B_1. An experimental correlation for B_1 is given in Equation 4.2 and shown in Figure 4.5.

$$\frac{h}{P} = B_1 \left(\frac{x}{P}\right)^{\frac{1}{2}} \tag{4.1}$$

$$B_1 = 0.42 \left[R\left(\frac{d}{H}\right)\right]^{\frac{1}{2}} \left(\frac{d}{L_\circ}\right)^{\frac{1}{4}} \tag{4.2}$$

It should be noted that in Equation 4.2 the initial wall jet diameter d is used to non-dimensionalize the height and length terms. This is used as a somewhat arbitrary length scale, as only one diameter was tested in these experiments. It is possible that another length-scale related to the initial turbulence or some sort of friction factor would be more appropriate for this correlation. The initial jet diameter is, however, quite commonly used in the literature for round jets in cross-flow as a scaling factor. Further research may find it to be a reasonable length scale. Despite the use of the jet diameter, Equation 4.2 provides a reasonable fit to the data shown in Figure 4.5, and provides a prediction of the measured coefficient with a maximum deviation of 25 percent.

The mid-field region falls within $0.12 < x/P < 0.25$. Within this region, the one-third power law fit (given in Equation 4.3) is used to characterize the jet's trajectory. This also matches the trajectory predictions given by Weil [19] and Briggs [23] in form, with different definitions of the experimentally defined coefficients. The experimental correlation for the coefficient B_2 is given in Equation 4.4 and the fit of this equation to the data is shown in Figures 4.6 and 4.7. This function is again dependent on d for convenience only. In this region, according to Weil [19], the jet is fully bent-over, and its trajectory is dominated by the cross-flowing fluid which it has entrained. The correlation defined in Equation 4.4 was found to predict the measured fit coefficients with a maximum difference of 34 percent. For low jet to cross-flow ratios, the jet's penetration is decreased and the recirculation zone has a greater impact on the jet's trajectory. In these cases, there is downward bending of the jet as shown by the $R = 5.8$ data in Figure 4.6. The models do not take this downward bending into account which leads to the maximum error being higher in the mid-field region

than in the near-field (where this effect does not take place).

$$\frac{h}{P} = B_2 \left(\frac{x}{P}\right)^{\frac{1}{3}} \tag{4.3}$$

$$B_2 = 0.31 \left[R \left(\frac{d}{H}\right) \left(\frac{d}{L_o}\right)^{0.5} \right]^{0.58} \tag{4.4}$$

The far-field region ($x/P > 0.25$) was found to be very erratic under the measurement conditions tested. This may have been due to the effects of the side walls, caused by the significant spreading of the jet in relation to the size of the water channel. At the top of the step the jet fluid had spread to fill a region greater than 20 cm in width (as shown in Figure 3.6). The width of the water channel was 68 cm. After the step, the jet continued to spread, and it grew closer to the side walls of the channel. At this point, portions of the jet may have interacted with the side walls which would alter the behaviour of the jet.

It appeared that the jet had entrained so much cross-flowing fluid that its vertical momentum was very small in relation to its horizontal momentum and the jet's rise was negligible. In some cases the jet stopped rising and began to fall (Figure 4.6). This is most likely due to the recirculation zone caused by the step [53] shown in Figure 4.8. Since the jet's momentum was dominated by the cross-flowing fluid, the downward bending of the cross-stream caused the jet's trajectory to bend downwards. Measurements were not taken

sufficiently far downstream to determine the exact cause of these effects. Thus, the final rise of the plume is not known for these experiments, and further experiments using a much smaller jet and step or a much larger water channel would be required in order to determine the final rise of the plume. The maximum rise can be approximated by using Equation 4.3 with $x/P = 0.25$.

4.3 Entrainment Model

An entrainment model was developed to better understand the physics of this problem, and to draw parallels between this flow and those flows which are more established in the literature. The trajectory of the round jet in cross-flow has been modeled with reasonable accuracy in the near field [19] and in the fully bent-over regions [23]. Weil [19] defines a momentum length scale, ℓ_m, which is given in Equation 4.5. This length scale is dependent on the jet velocity (V_{jet}), the cross-flow velocity (V_∞), and the radius of the initial round jet entering the cross-flow (r_o). Using this length scale, the trajectory models presented by Weil [19] for the near-field and fully bent-over regions are given in Equations 4.6 and 4.7 which show the height of the jet (h) based on the distance from the jet's source (x). Here R^* represents the velocity ratio comparing the vertical jet entering the cross-flow with the local velocity of the cross-flow which the jet entrains. The two coefficients, α and β are defined as 0.11 and 0.6 respectively for round jets in cross-flow. It will be assumed that these are reasonable estimates for all jets in cross-flow for the development of the entrainment model.

$$\ell_m = \frac{\rho_o}{\rho_a}^{1/2} \frac{V^*_{jet}}{V^*_\infty} r_o \tag{4.5}$$

$$\frac{h}{\ell_m} = \left(\frac{R^*}{\alpha R^* + \beta}\right)^{\frac{1}{2}} \left(\frac{x}{\ell_m}\right)^{\frac{1}{2}} \tag{4.6}$$

$$\frac{h}{\ell_m} = \left(\frac{3}{\beta^2}\right)^{\frac{1}{3}} \left(\frac{x}{\ell_m}\right)^{\frac{1}{3}} \tag{4.7}$$

In order to use the round jet model to characterize the elliptical jet in cross-flow presented in this study, an equivalent value for each term is required. The two difficult parameters to determine are the velocity ratio (R^*) and the source radius (r_o). Since the local velocity of the vertical jet was not measured, it was approximated through the use of conservation equations (mass flux and momentum flux given in Equations 4.8 and 4.9 (derived in Appendix C)) and was found to be dependent on the shape and cross-sectional area of the vertical jet, as well as the losses present below the lip of the step. The cross-flow velocity was calculated at a location midway between the step and the maximum plume rise using the velocity profile measured by Hilderman [40] given in Equation 2.1 which assumes that the boundary layer has not yet been effected by the step. Based on these velocities, the velocity ratio R^* is defined as shown in Figure 4.9. The source radius (r_o) is typically half of the thickness of the jet cross section. For a round jet this represents the radius of the jet, and for an elliptical jet it was assumed to be half of the minor axis of the ellipse.

$$\rho_1 V_1 A_1 = \rho_2 V_2 A_2 \tag{4.8}$$

$$\rho_1 A_1 V_1^2 = \frac{1}{2} C_D \rho_1 A_1 V_1^2 + \rho_2 A_2 V_2^2 \tag{4.9}$$

The simplest and most apparent model for this system would be to assume the horizontal wall jet was directed vertically without changing shape or losing momentum. In this case, the vertical jet would have both the same speed and radius as the initial wall jet. The round jet case is shown as the round jet with no drag in Figure 4.10. From this figure it can be seen that the over-prediction of the rise is very significant and unrealistic. To improve the accuracy of the model, the cross-sectional area of the vertical jet was set to match the area of the ellipse measured in Chapter 3. For this case it was assumed that the change in the jet's momentum was caused by drag losses which the jet experienced as it traveled along the floor of the channel. The trajectory of the assumed round vertical jet (shown as round jet with drag) is shown in Figure 4.10. The friction losses were found to have a drag coefficient of 1.6 for this case. Based on these findings, it can be seen that simplifying the model to a round jet with the measured area under-predicts the entrainment of cross-flowing fluid and leads to over-prediction of the maximum rise. To improve the accuracy of the model, it is apparent that the elliptical shape measured in Chapter 3 must be incorporated into the model. Figure 4.11 shows a comparison of a round vertical jet with an elliptical vertical jet (with r_o defined as half the length of the minor axis) which

both have the same cross-sectional area. In both cases the losses are due to a drag force with a coefficient of 1.6. The use of the elliptical cross-section significantly improves the fit of the model to the experimental trajectory data.

It can be argued that as the wall jet travels along the floor and the fluid impinges onto the step, it entrains surrounding fluid which leads to an increase in the mass flow of the jet, causing the jet's mean velocity to decrease. This entrainment assumption does explain both the spread and the change in velocity of the fluid. To determine the effect of this entrainment, the trajectory of this jet was determined by assuming that there was no drag force (so the momentum flux of the initial jet and the jet entering the cross-flow were equal), and the decrease in velocity was caused by the addition of mass into the flow. The effect of this assumption on the jet's trajectory is shown in Figure 4.12.

It was also assumed that the momentum losses were due entirely to a drag force, and the effects of the step geometry on the drag coefficient were analyzed. Figure 4.12 shows a comparison between the trajectory of the jet assuming entrainment with the trajectory assuming a drag coefficient of 1.6. In this case it is apparent that the drag force explains the losses in the flow better than entrainment. Figure 4.13 shows the effect of the velocity ratio on the calculated drag coefficient, which appears to have little effect. The drag coefficient is more strongly influenced by the geometry of the step as shown in Figure 4.14. From this it appears that using the elliptical cross section, with r_o defined as half of the minor axis of the ellipse, and assuming that the changes in jet shape and velocity before the top of the step are caused by drag forces lead to the most accurate prediction of the jet trajectory.

The entrainment coefficients for the round jet model were determined from the jet trajectory measurements. Through manipulating equations 4.3 and 4.7, and equating the jet height h yields:

$$\beta = \left(\frac{3}{B_2^3}\right)^{1/2} \frac{\ell_m}{P} \tag{4.10}$$

Equation 4.5 can be substituted for ℓ_m while assuming constant density in the flow. Also, the source radius r_o can be approximated by taking half of the minor axis of the ellipse (D). Substituting these yields a relationship for β (shown in equation 4.11) based on the empirical curve fits used to develop equation 4.3. A similar relationship was used to determine α based on equations 4.1 and 4.6.

$$\beta = \left(\frac{3}{B_2^3}\right)^{1/2} R^* \left(\frac{D}{2P}\right) \tag{4.11}$$

The values of α and β were determined for each test to determine if the constant values given by Weil [19] for the round jet case were reasonable values to use for the elliptical jet. Figure 4.15 shows the dependence of α on the velocity ratio. The average value of α was found to be 0.15 with a standard deviation of 0.13, and it appears to have a slight dependence on R^*. However, with the large amount of scatter, it is possible that the value approaches the average presented by Weil [19] of $\alpha = 0.11 \pm 0.02$. From Figure 4.16 it can be seen that the value of β is not dependent on the velocity ratio. The average value of

β was found to be 0.58, with a standard deviation of 0.14. The average value presented by Weil [19] is $\beta = 0.6 \pm 0.15$, which agrees with the value measured by these experiments. Figure 4.17 gives the two curve fits using Equations 4.6 and 4.7 for a single jet trajectory image. This figure shows the accuracy of the trajectory predicted using the entrainment model. It shows a reasonable fit in the near-field and bent-over jet region, but in the far stream it over-predicts the final plume rise. Further experiments and modifications are required to predict the jet behaviour further downstream. This entrainment model should be used to predict the maximum possible plume rise, and the final rise may be lower than the one predicted by the model. The large scatter in the entrainment coefficients shows that assuming that they are constant may lead to significant errors in the trajectory predictions.

The models presented in this section have attempted to use the round jet model and entrainment coefficients to predict the trajectory of the elliptical jet. A new model was developed to accurately predict the elliptical jet's trajectory using the round jet entrainment constants, by approximating the elliptical jet as a round jet with a diameter equal to the ellipse's *minor* axis. This was because the elliptical jet entrains more fluid than the round jet, and a model for a round jet of equal area using the standard entrainment coefficient significantly over-predicts the jet's rise as shown in Figure 4.10.

Appendix B shows how the Briggs trajectory model [54] can be modified for an elliptical jet with a constant aspect ratio. The modified rise equation from Appendix B is shown in Equation 4.12. This produces a new entrainment constant β_e which represents the trajectory-averaged entrainment coefficient which a round jet with the same cross-sectional

area as the elliptical jet would have to experience in order to entrain the same amount of surrounding fluid as the elliptical jet. This new constant β_e is defined in Equation 4.13. Table 4.1 shows the values of β_e calculated assuming a constant aspect ratio. The values of β_e are larger than the round jet values of β. This shows that the elliptical jet has more entrainment than the round jet, which decreases its penetration into the cross-flowing fluid.

$$z_c' = \sqrt[3]{\frac{8}{3}}\sqrt[3]{\frac{3F_m x}{U^2\beta^2}}\left(\frac{1}{S^2+2S+3}\right)^{1/3} \tag{4.12}$$

$$\beta_e^2 = \frac{3\beta^2}{8}\left(\frac{S^2+\frac{2}{3}S+1}{S}\right) \tag{4.13}$$

An actual impinging jet does not have a constant aspect ratio. After impingement, it appeared to bend into a 'horse-shoe' shape which lowered its aspect ratio and made the jet become more circular. This model shows the effect of an elliptical cross-section with constant aspect ratio, and if the shape of the jet were known within the bent-over region this could improve predictions of the trajectory of elliptical jets.

4.4 Conclusion

This study has presented two methods of predicting the trajectory of an elliptical jet in cross-flow formed by a wall jet impinging onto a forward facing step. In both cases the flow contained three regions: a near-field region dominated by the initial jet momentum, a fully bent-over region where the cross-flowing fluid has been entrained, and a far-field region where the jet has stopped rising. In the near-field region a power law fit with an exponent of 1/2 was found to best fit the trajectory data. In the fully bent-over region, the exponent

to the power law was 1/3. This is consistent with the round jet in cross-flow models given in [23] and [19]. In the far-field, the jet's rise became negligible and in some cases the jet fell below its maximum rise. This was most due to a recirculation zone over the step changing the velocity profile of the cross-flowing fluid. In the fully bent over region, the model may continue to define the jet trajectory further downstream for cases where the streamlines of the cross-flow do not have such a strong recirculation region.

Two models were presented: one based on empirical results, and one based on entrainment theory. The first model used experimental correlations relating the jet's inlet velocity ratio and the step's geometry to the experimental curve fit. The second model used a modified version of the entrainment models presented by Weil [19] and Briggs [23] for round jets. The mean values of the entrainment coefficients for the round jets were found to be within the uncertainty of the mean values calculated for the elliptical jet model. It was also determined that in the wall jet region, the spreading of the jet was dominated by a drag force with an average drag coefficient of 1.6. Based on the scatter in the entrainment coefficients for the entrainment model, the empirical models appear to better predict the jet trajectories (for all of the measured cases) and as such should be used for jet predictions.

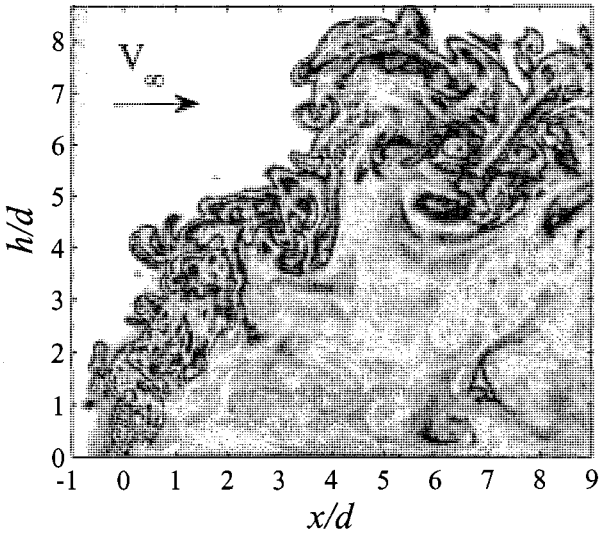

Figure 4.1: Single jet image used for trajectory measurements. The concentration profile along the jet centerline is represented by a sawtooth function to emphasize the flow structures. The axes show the height above the step (h) against the distance from the step (x) both normalized with the initial jet diameter (d).

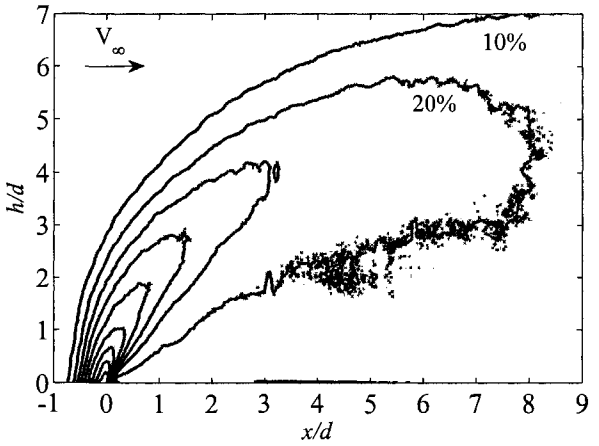

Figure 4.2: Contour plot of the concentration of an averaged jet used for jet trajectory measurements. Contours vary from 10 to 90 percent of the maximum jet concentration. Axes represent the height above the step (h) versus the horizontal distance from the step (x) both normalized with the initial jet diameter (d).

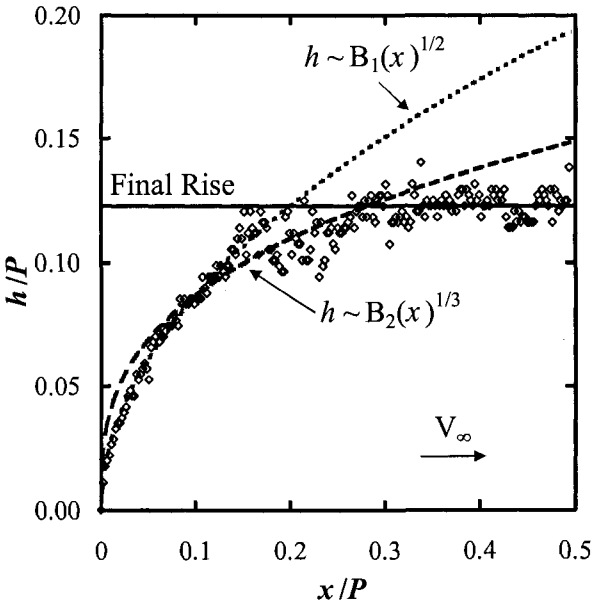

Figure 4.3: Curve fits for a single jet trajectory measurement. The $h \backsim x^{1/2}$ fit is valid for $0 < x/P < 0.12$, the $h \backsim x^{1/3}$ fit is valid for $0.12 < x/P < 0.25$. The complete relationships are shown in Equations 4.1 and 4.3. The final rise is also approximated.

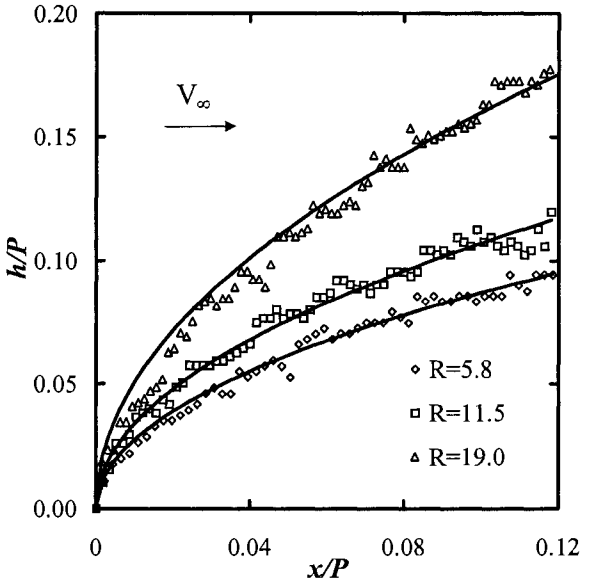

Figure 4.4: Curve fits for the $h \backsim B_1(x)^{1/2}$ power law relationship used to determine the constant B_1 fitted for three velocity ratios within $0 < x/P < 0.12$. These tests used a single step height and distance from the step. Jet penetration increases significantly with increasing jet to cross-flow velocity ratio.

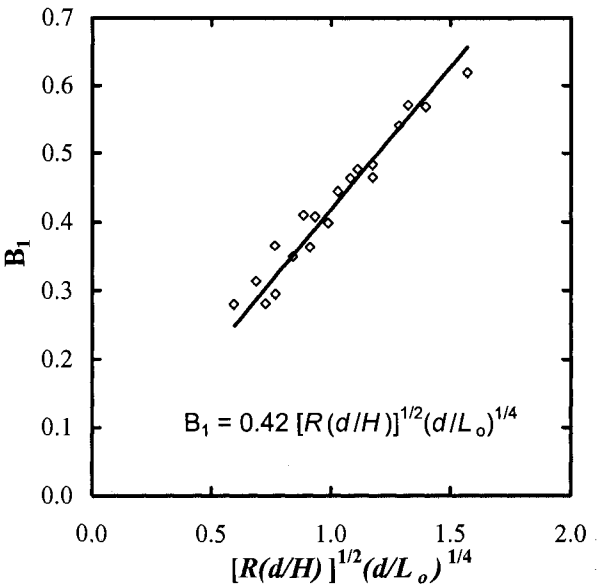

Figure 4.5: Determination of B_1 from $h \backsim B_1(x)^{1/2}$ in terms of the velocity ratio R, the step height H, the jet diameter d and the effective distance to the step L_o.

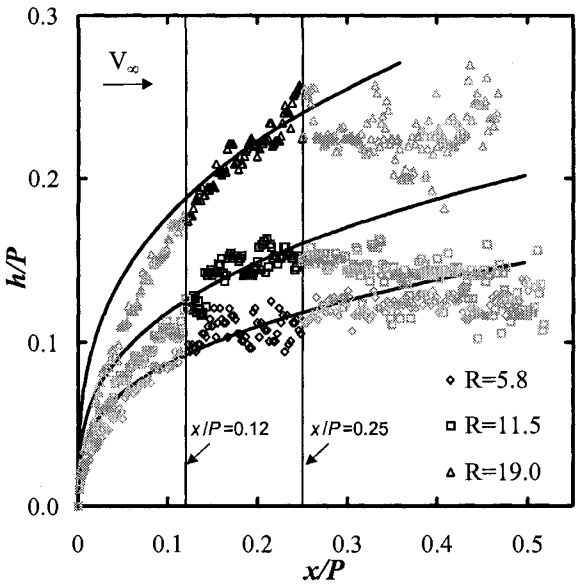

Figure 4.6: Curve fits for the $h \backsim \mathrm{B}_2(x)^{1/3}$ power law relationship used to determine the constant B_2 fitted for three velocity ratios within $0.12 < x/P < 0.25$. These tests used a single step height and distance from the step. Jet penetration increases significantly with increasing jet to cross-flow velocity ratio. Further downstream than $x/P = 0.25$ the cross-flow momentum dominates, and in some cases the jet bends towards the floor of the channel.

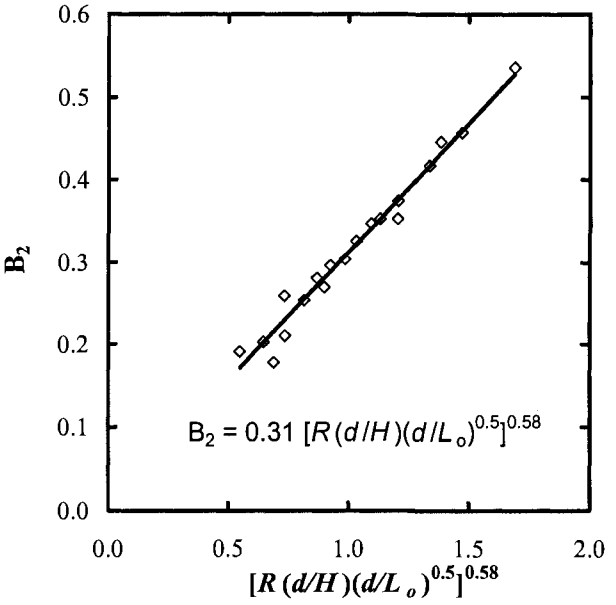

Figure 4.7: Determination of B_2 from $h \backsim (\mathrm{B}_2 x)^{1/3}$ in terms of the velocity ratio R, the step height H, the jet diameter d, and the effective distance to the step $L_\circ$.

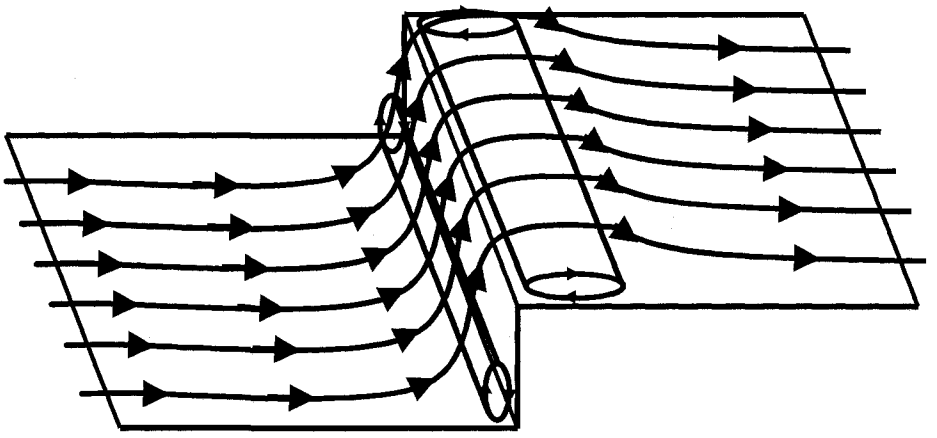

Figure 4.8: Recirculation zone above the step which leads to downward bending of the cross-flowing fluid streamlines [53].

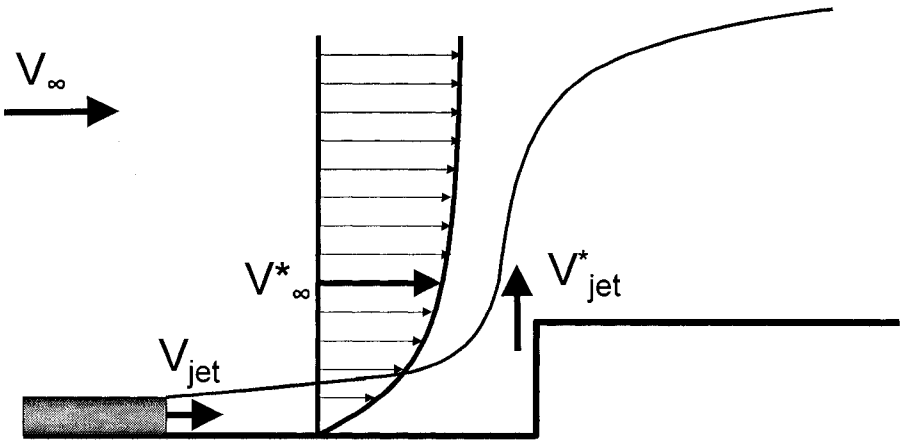

Figure 4.9: Parameters used to determine velocity ratios. Here $R = V_{jet}/V_\infty$ and $R^* = V^*_{jet}/V^*_\infty$.

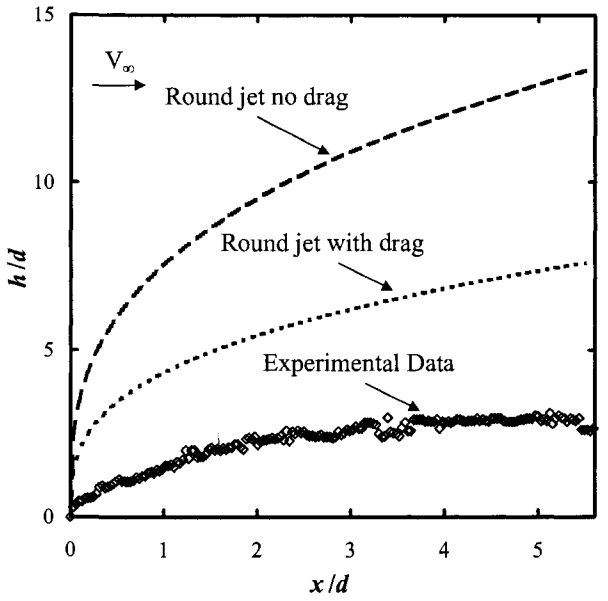

Figure 4.10: Predicted jet trajectories assuming that the jet entering the cross-flow is circular. The first curve represents the case with no drag and no shape change. The second curve uses a round jet with a drag coefficient of 1.6 which was calculated from the measured elliptical jet's cross-sectional area. Both cases use an entrainment coefficient of $\beta = 0.6$.

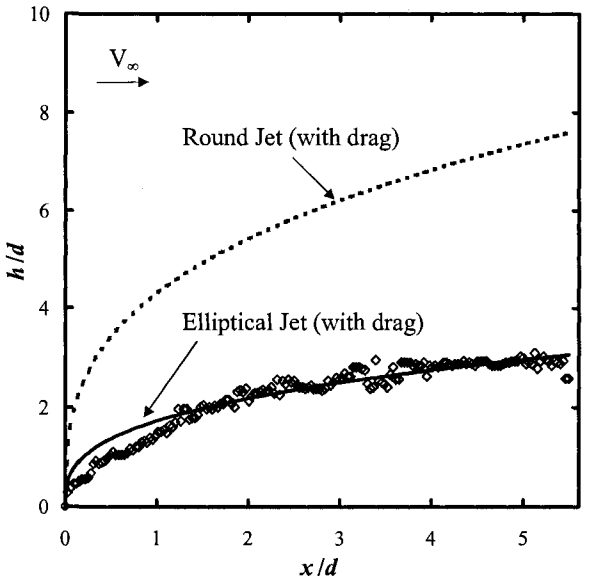

Figure 4.11: Effect of the jet shape on its trajectory. The trajectories were calculated assuming the shape of the jet entering the cross-flow was round and elliptical. Both jets had the same area and their calculated drag coefficients were both 1.6.

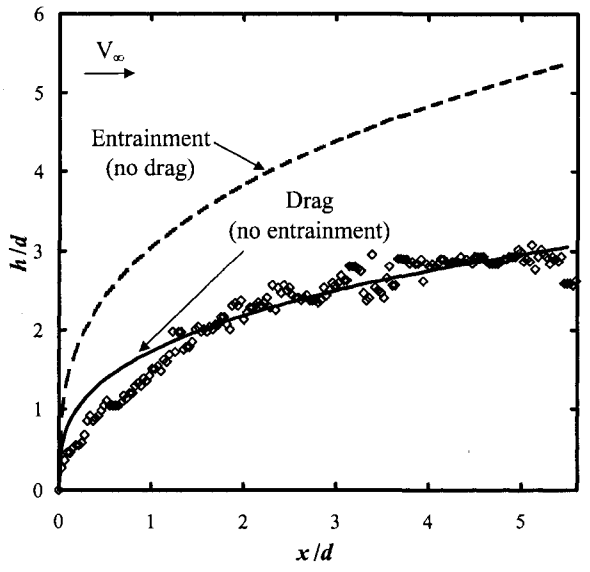

Figure 4.12: Jet trajectories calculated assuming that the jet's trajectory is determined by drag and entrainment. Both trajectories assume an entrainment coefficient in the cross-flow of $\beta = 0.6$. The drag cases uses a calculated drag coefficient of 1.6.

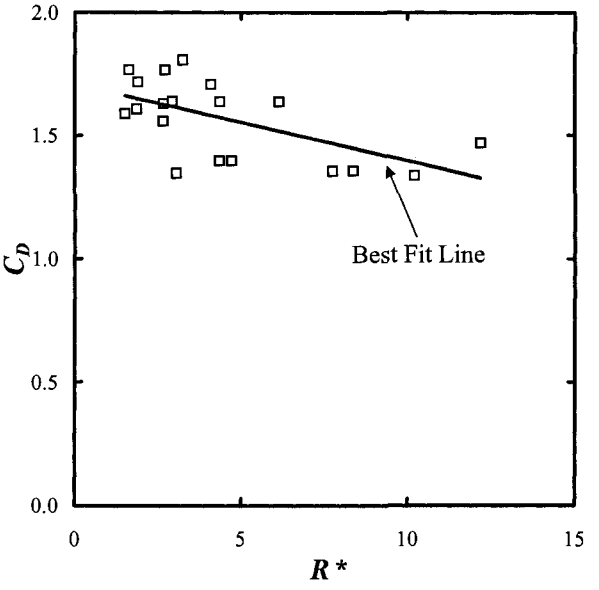

Figure 4.13: Effect of the local velocity ratio (R^*) on the calculated drag coefficient (C_D). The trend is weak and may be due to scatter in the data.

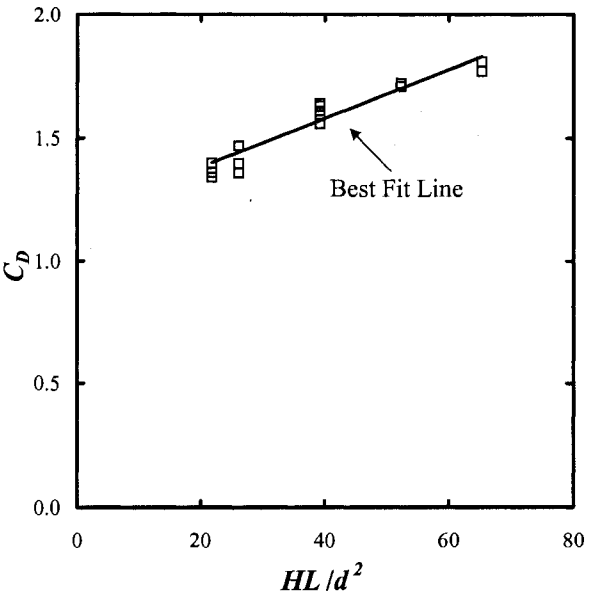

Figure 4.14: Effect of the step position (L) and height (H) on the calculated drag coefficient. The increase in HL increases the surface area which the jet travels over before entering the cross-flow, increasing the momentum loss due to drag.

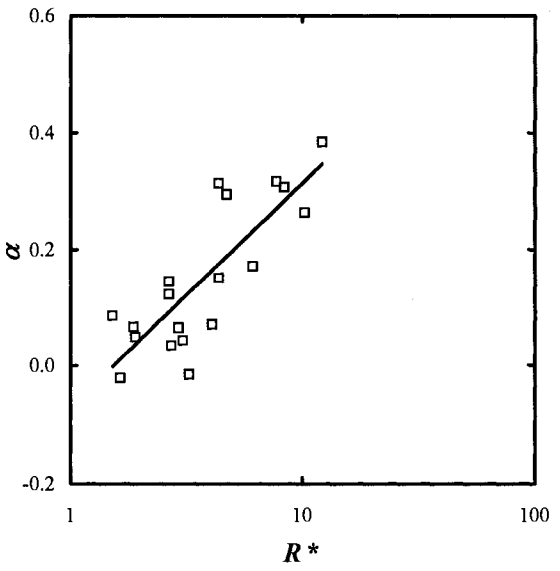

Figure 4.15: Entrainment coefficient α given in Equation 4.6 ($h \backsim x^{1/2}$) for the near-field region for the jet. The value presented in Weil [19] is constant with $\alpha = 0.11$. Here, the average is $\alpha = 0.15$ with a standard deviation of 0.13.

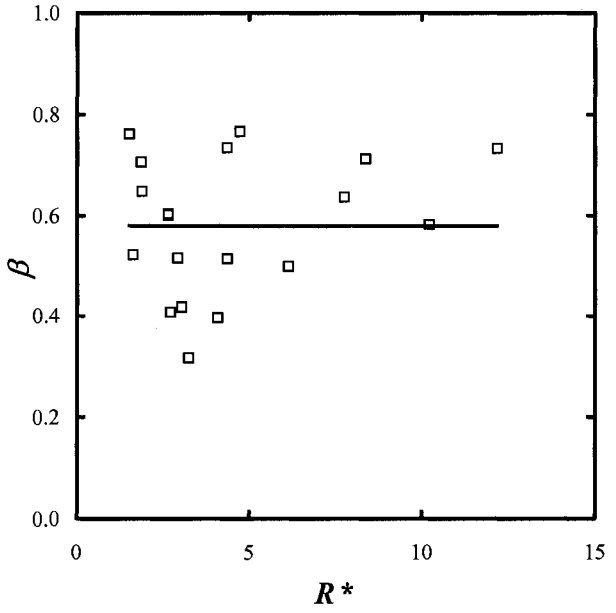

Figure 4.16: Entrainment coefficient β for the fully bent over region of the jet calculated using Equation 4.7 ($h \backsim \beta^{-2/3} x^{1/3}$). The value given in Briggs [23] and Weil [19] is $\beta = 0.6$. Here the mean is $\beta = 0.58$ (shown with the horizontal line) with a standard deviation of 0.14.

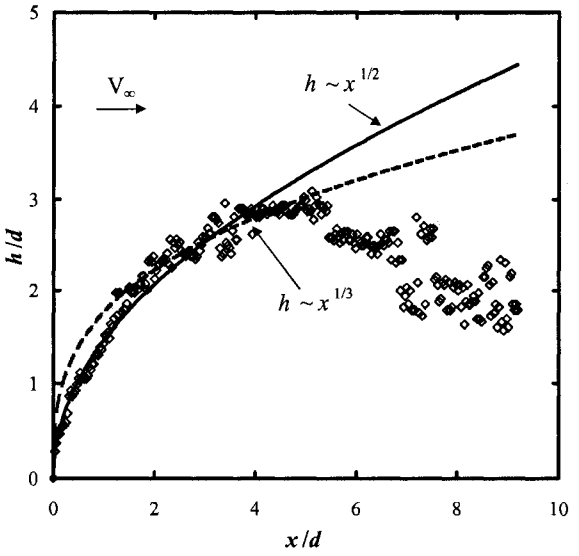

Figure 4.17: Curve fits using the average values of $\alpha = 0.15$ and $\beta = 0.58$ for a single jet using $h \backsim (\alpha, \beta)\ x^{1/2}$ and $h \backsim \beta^{-2/3}\ x^{1/3}$. In the far-field region, the bending streamlines in the cross-flow due to the recirculation over the step [53] cause the jet to bend towards the floor of the channel.

Table 4.1: Effect of aspect ratio on the elliptical entrainment coefficient β_e.

S	βe
1	0.60
2	0.65
3	0.73
5	0.89
10	1.21
15	1.46
20	1.67
50	2.62

Chapter 5

Conclusion

5.1 Summary

Empirical and theoretical models for predicting the behaviour of a jet impinging onto a forward facing step have been presented. These models may be useful in improving hazard assessment models for the rupture of buried pipelines. The specific conclusions of the study are presented below.

1. The perimeters and aspect ratios of the elliptical jets entering vertically into the cross-flow can be approximated using empirical scaling laws based on the initial step height, the effective distance from the jet to the step, and the jet to cross-flow velocity ratio.

2. A simple k-ϵ solution to the RANS equations can be used to give an approximation for the jet shape and provide reasonable approximations for the trends in the presented parametric study.

3. Jet trajectories can be modeled using empirical power law fits with exponents of 1/2

in the near field and 1/3 further downstream. The coefficients of these power law fits are dependent on the perimeter of the jet emitted into the cross-flow, the step height, the distance to the step, and the velocity ratio. The maximum rise of the jet can be approximated using the 1/3 power law fit at $x/P = 0.25$.

4. The Briggs round jet entrainment models can be used to predict the jet trajectory with average coefficients of $\beta = 0.58 \pm 0.14$ and $\alpha = 0.15 \pm 0.13$.

5. The jet-step interaction can be modeled with a a drag force with a coefficient $C_D = 1.6$ and a shape change from a round jet to an elliptical jet with a known perimeter and aspect ratio.

5.2 Future Work

Future work is required to better understand this geometry and to more accurately expand the application of this study to underground pipeline ruptures. Some projects which could be undertaken are outlined below.

1. Enhance CFD models to predict the jet trajectories through the use of finer grids with mesh refinement downstream of the step. These models could be used to test a wider variety of parameters and study specific cases of pipeline ruptures.

2. Determine the range of applicability of the scaling relationships presented in this study by further varying the velocity ratio, step height, and distance to the step. From this, the limiting parameters can be discovered.

3. Use various jet diameters to further justify the use of d in the scaling relationships

and to determine the effects of Reynolds number on the flow.

4. Determine the effects of back and side crater walls on both the drag coefficient and the shape of the jet entering the cross-flow.

5. Analyze the trajectory of the jet far downstream from the step. From this, a more accurate model of the final rise for the jet could be produced.

Bibliography

[1] J.D. Whittaker, R.P. Angle, D.J. Wilson, and M.G. Choukalos. Risk-based zoning for toxic-gas pipelines. *Risk Analysis*, 2(3):163–169, 1982.

[2] D. J. Wilson. The release and dispersion of gas from pipeline ruptures. Technical report, Alberta Environment, 1979.

[3] D. J. Wilson. Expansion and plume rise of gas jets from high pressure pipeline ruptures. Technical report, Alberta Environment, 1981.

[4] B.E. Launder and W. Rodi. The turbulent wall jet. *Progress in Aerospace Sciences*, 19:81–128, 1981.

[5] T.J. Craft and B.E. Launder. On the spreading mechanism of the three-dimensional turbulent wall jet. *Journal of Fluid Mechanics*, 435:305–326, 2001.

[6] M.R. Davis and H. Winarto. Jet diffusion from a circular nozzle above a solid plane. *Journal of Fluid Mechanics*, 101(1):201–221, 1980.

[7] D.J. Phares, G.T. Smedley, and R.C. Flagan. The inviscid impingement of a jet with arbitrary velocity profile. *Physics of Fluids*, 12(8):2046–2055, 2000.

[8] C.D. Donaldson and R. S. Snedeker. A study of free jet impingement. Part 1. Mean properties of free and impinging jets. *Journal of Fluid Mechanics*, 45(2):281–319, 1971.

[9] L. Song and J. Abraham. The structure of wall-impinging jets: computed versus theoretical and measured results. *Journal of Fluids Engineering*, 125:997–1005, November 2003.

[10] M. Bouainouche, N. Bourabaa, and B. Desmet. Numerical study of the wall shear stress produced by the impingement of a plane turbulent jet on a plate. *International Journal of Numerical Methods for Heat and Fluid Flow*, 7(6):548–564, 1997.

[11] K. Nishino, M. Samada, K. Kasuya, and K. Torii. Turbulence statistics in the stagnation region of an axisymmetric impinging jet flow. *International Journal of Heat and Fluid Flow*, 17:193–201, 1996.

[12] L. Song and J. Abraham. Entrainment characteristics of transient turbulent round, radial and wall-impinging jets: Theoretical deductions. *Journal of Fluids Engineering*, 125:605–612, July 2003.

[13] R.J. Margasson. Fifty years of jet in crossflow research. *AGARD Symposium on a Jet in Cross Flow*, Winchester, UK, AGARD CP-534, 1993.

[14] S. Muppidi and K. Mahesh. Study of trajectories of jets in crossflow using direct numerical simulations. *Journal of Fluid Mechanics*, 530:81–100, 2005.

[15] S. H. Smith and M. G. Mungal. Mixing, structure and scaling of the jet in crossflow. *Journal of Fluid Mechanics*, 357:83–122, 1998.

[16] Y. Kamotani and I. Gerber. Experiments on turbulent jet in a crossflow. *AIAA Journal*, 10(11):1425–1429, 1972.

[17] L.L. Yuan and R. L. Street. Trajectory and entrainment of a round jet in crossflow. *Physics of Fluids*, 10(9):2323–2335, 1998.

[18] J. E. Broadwell and R. E. Breidenthal. Structure and mixing of a transverse jet in incompressible flow. *Journal of Fluid Mechanics*, 148:405–412, 1984.

[19] J. C. Weil. Plume rise. In A. Venkatram and J. C. Wyngaard, editors, *Lectures on Air Pollution Modeling*, pages 119–162. American Meteorological Society, 1988.

[20] T. H. New, T. T. Lim, and S. C. Luo. A flow field study of an elliptic jet in cross flow using DPIV technique. *Experiments in Fluids*, 36:604–618, 2004.

[21] T. H. New, T. T. Lim, and S. C. Luo. Elliptic jets in cross-flow. *Journal of Fluid Mechanics*, 494:119–140, 2003.

[22] T. T. Lim, T. H. New, and S. C. Luo. Scaling of trajectories of elliptic jets in crossflow. *AIAA Journal*, 44(12):3157–3160, 2006.

[23] G.A. Briggs. Plume rise predictions. In D.A. Haugen, editor, *Lectures on air pollution and environmental impacts analysis*, pages 59–111. American Meteorological Society, Boston, 1975.

[24] G.A. Davidson. Simultaneous trajectory and dilution predictions from a simple integral plume model. *Atmospheric Environment*, 23(2):341–349, 1989.

[25] D. A. Walker. A fluorescence technique for measurement of concentration in mixing liquids. *Journal of Physics E: Scientific Instrumentation*, 20:217–224, 1987.

[26] Sadtler Research Laboratories. *Sadtler Standard Spectra.* 1974.

[27] M.M. Martin and L. Lindqvist. The pH dependence of fluorescein fluorescence. *Journal of Luminescence*, 10:381–390, 1975.

[28] M.C. Mota, P. Carvalho, J. Ramalho, and E. Leite. Spectrophotometric analysis of sodium fluorescein aqueous solutions. determination of molar absorption coefficient. *International Opthamology*, 15:321–326, 1991.

[29] L.G. Larsen and J.P. Crimaldi. The effect of photobleaching on PLIF. *Experiments in Fluids*, 41:803–812, 2006.

[30] J. Crimaldi. The effect of photobleaching and velocity fluctuations on single-point LIF measurements. *Experiments in Fluids*, 23:325–330, 1997.

[31] J.P. Crimaldi and J.R. Koseff. High-resolution measurements of the spatial and temporal scalar structure of a turbulent plume. *Experiments in Fluids*, 31:90–102, 2001.

[32] I. Powell. Design of a laser beam line expander. *Applied Optics*, 26(17):3705–3709, 1987.

[33] S.B. Pope. *Turbulent Flows.* Cambridge University Press, New York, 2000.

[34] K. Hanjalić. Advanced turbulence closure models: a view of current status and future prospects. *International Journal of Heat and Fluid Flow*, 15(3):178–203, 1994.

[35] B.E. Launder and B.I. Sharma. Application of the energy-dissipation model of turbulence to the calculation of flow near a spinning disk. *Letters in Heat and Mass Transfer*, 1:131–138, 1974.

[36] R. A. Cusworth and J. P. Sislian. Computation of turbulent free isothermal swirling jets. Technical Report 315, University of Toronto Institute for Aerospace Studies, 1987.

[37] K. Kalita, A. Dewan, and A. K. Dass. Prediction of turbulent plane jet in crossflow. *Numerical Heat Transfer, Part A*, 41:101–111, 2002.

[38] J. Kechiche, H. Mhiri, G. Le Palec, and P. Bournot. Application of low Reynolds number $k - \epsilon$ turbulence models to the study of turbulent wall jets. *International Journal of Thermal Sciences*, 43:201–211, 2004.

[39] P. J. Roache. Quantification of uncertainty in computational fluid dynamics. *Annual Review of Fluid Mechanics*, 29:123–160, 1997.

[40] T.L. Hilderman and D.J. Wilson. Predicting plume meandering and averaging time effects on mean and fluctuating concentrations in atmospheric dispersion simulated in a water channel. *Boundary-Layer Meteorology*, 122:535–575, 2007.

[41] K. Shahzad, B.A. Fleck, and D.J. Wilson. Small scale modeling of vertical surface jets in cross-flow: Reynolds number and downwash effects. *Journal of Fluids Engineering*, 129:311–318, 2007.

[42] C.R. Johnston and D.J. Wilson. A vortex pair model for plume downwash into stack wakes. *Atmospheric Environment*, 31(1):13–20, 1997.

[43] T.L. Hilderman. *Measurement, modelling, and stochastic simulation of concentration fluctuations in a shear flow.* PhD thesis, University of Alberta, 2004.

[44] Kodak. *Photographic Filters Handbook.* Eastman Kodak Company, 1990.

[45] J.H. Yoon and S.J. Lee. Investigation of the near-field structure of an elliptic jet using stereoscopic particle image velocimetry. *Measurement Science and Technology*, 14:2034–2046, 2003.

[46] G. P. Michon. Final answers: Perimeter of an ellipse. *numericana.com*, updated May 27 2008. Accessed June 9 2008. < *www.numericana.com/answer/ellipse.htm* >.

[47] M. Behnia, S. Parneix, and P. A. Durbin. Prediction of heat transfer in an axisymmetric turbulent jet impinging on a flat plate. *International Journal of Heat and Mass Transfer*, 41(12):1845–1855, 1998.

[48] B.E. Launder and Spalding D.B. Numerical computation of turbulent flows. *Computer Methods in Applied Mechanics and Engineering*, pages 269–289, 1990.

[49] H. Grotjans and F. Menter. Wall functions for general application CFD codes. In *Proceedings of 4th European Computational Fluid Dynamics Conference, Athens, Greece*, volume 1, pages 1112–1117. John Wiley and Sons, 1998.

[50] G. de Vahl Davis. Natural convection of air in a square cavity: a bench mark numerical solution. *International Journal for Numerical Methods in Fluids*, 3:249–264, 1983.

[51] C. A. J. Fletcher. *Computational Techniques for Fluid Dynamics*, volume 1. Springer-Verlag, 2nd edition, 1991.

[52] P. Andreasson and U. Svensson. A note on a generalized eddy-viscosity hypothesis. *Journal of Fluids Engineering*, 114:463–466, 1992.

[53] J. G. Barbosa-Saldana and N. K. Anand. Flow over a three-dimensional horizontal forward-facing step. *Numerical Heat Transfer, Part A: Applications*, 53:1–17, 2008.

[54] G. A. Briggs. *Atmospheric Science and Power Production Chapter 8: Plume Rise and Buoyancy Effects.* United States Department of Energy, 1984.

[55] J. H. W. Lee and V. Chu. *Turbulent Jets and Plumes: A Lagrangian Approach.* Springer, 2003.

Appendix A

Rotameter Calibration

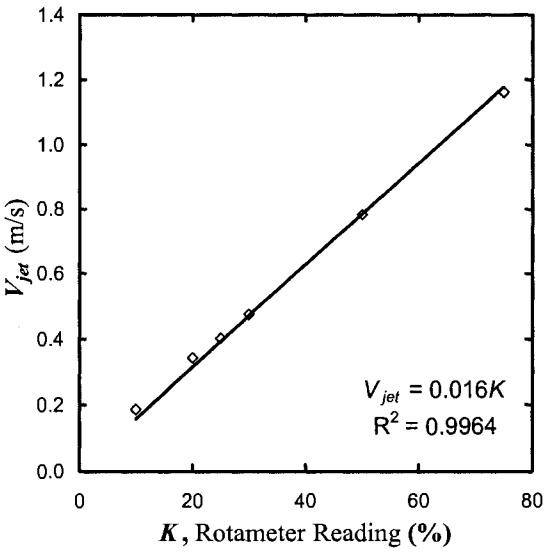

Figure A.1: Calibration curve for rotameter RA-001.

Appendix B

Fully-Bent-Over Jet Rise Model for an Elliptical Plume Cross Section with Constant Aspect Ratio and Entrainment Coefficient

The bent over plume entrainment model presented by Briggs [23] assumes that the jet entering the cross-flow begins as a round jet and remains that shape along its entire trajectory. The vertical jet presented in this study begins as a high aspect ratio elliptical jet. The entrainment model presented in the main text of the thesis assumes that the trajectory of the elliptical jet can be predicted using the round jet model, with an effective radius equal to half of the minor axis of the ellipse (as defined in Chapter 4). The use of this model is justified by the assumption that the jet's behaviour can be approximated by the two dimensional case, where twice the radius of the round jet and the minor axis of the ellipse are the same quantity. As the elliptical jet is deflected in the cross-flow, it appears to 'roll-up' due to the counter-rotating vortex pair into a horseshoe shape and then eventually into a more circular shape. The shape change further justifies using the round jet model. However, for cases where the jet's aspect ratio remains high, a modified version of the Briggs [23] model would more accurately predict the entrainment and trajectory of the jet.

The Briggs model [23] can be modified for an elliptical jet, assuming that the aspect ratio of this jet remains constant throughout its trajectory. Based on experimental observations this is not the case for the jet impinging on the step, however, it gives a representation of the effects of the non-circular shape. Through manipulating the equations presented by Briggs [54], the analysis below shows the effect of the elliptical shape on the entrainment coefficient and the trajectory of the jet.

Briggs [54] defines the volume flux (V) as:

$$V = \pi r^2 U \tag{B.1}$$

For a bent-over plume, Briggs [54] shows:

$$\frac{dV}{dz'_c} = 2\pi r \beta U \tag{B.2}$$

Using area (A) and perimeter (P) for a more general case of a jet with arbitrary shape:

$$V = UA \tag{B.3}$$

$$\frac{dV}{dz'_c} = P\beta U \tag{B.4}$$

Differentiating Equation B.3 with respect to the vertical distance from the source (z'_c), and combining with Equation B.4 yields:

$$\beta = \frac{1}{P}\frac{dA}{dz'_c} \tag{B.5}$$

Assuming the jet is elliptical in shape with a major axis (a_1) and a minor axis (a_2) which have an aspect ratio (S) which remains constant. Where:

$$S = \frac{a_1}{a_2} \tag{B.6}$$

The area of an ellipse is:

$$A = \pi a_1 a_2 = \pi S a_2^2 \tag{B.7}$$

A simple approximation for the perimeter of an ellipse is given in Equation 2.3 [46], and can be modified using the jet's aspect ratio to produce:

$$P = \sqrt{\frac{3}{2}}\pi a_2 (S^2 + \frac{2}{3}S + 1)^{1/2} \tag{B.8}$$

Assuming that the aspect ratio is constant, Equation B.5 becomes:

$$\beta = \sqrt{\frac{8}{3}}\left(\frac{S}{(S^2 + \frac{2}{3}S + 1)^{1/2}}\right)\frac{da_2}{dz'_c} \tag{B.9}$$

A new constant (K) can be defined such that:

$$\frac{1}{K} \equiv \sqrt{\frac{8}{3}} \left(\frac{S}{(S^2 + \frac{2}{3}S + 1)^{1/2}} \right) \tag{B.10}$$

Using the momentum conservation equation and the closure model from Equation B.5 [54] yields:

$$z_c' = \sqrt[3]{\frac{3F_m x}{U^2 \beta^2}} \sqrt[3]{\frac{1}{SK^2}} \tag{B.11}$$

Where F_m is the source value of the momentum flux. Replacing the K term gives:

$$z_c' = \sqrt[3]{\frac{8}{3}} \sqrt[3]{\frac{3F_m x}{U^2 \beta^2}} \left(\frac{S}{S^2 + \frac{2}{3}S + 1} \right)^{1/3} \tag{B.12}$$

Equation B.11 represents a modified version of the 1/3 power law fit presented by Briggs [23] (which is equivalent to Equation 4.7). The only difference between the round jet model equation and the elliptical jet model equation is the last term in Equation B.11. This difference leads to a scaling value which is dependent on the aspect ratio of the jet. For the case of a round jet, this SK^2 term is equal to one, and the equation reverts to the round jet case.

A new entrainment coefficient (β_e) can be defined as the trajectory-averaged entrainment coefficient that a round jet with the same cross-sectional area as the elliptical jet would have to experience in order to entrain the same amount of surrounding fluid as the elliptical jet. This coefficient is defined in equation B.13.

$$\beta_e = \frac{1}{SK^2 \beta^2} \tag{B.13}$$

Assuming that the initial entrainment coefficient (β) is equal to 0.6, the effect of the aspect ratio can be determined. Table B.1 shows the effect of the aspect ratio on the trajectory

$(1/SK^2)$ and the entrainment coefficient (β_e). In both cases it is assumed that the aspect ratio remains constant throughout the jet's trajectory. Comparing the values of β_e with the entrainment coefficients calculated earlier (shown in Figure 4.16) shows that the assumption of a constant aspect ratio fails for the impinging jet case.

Table B.1: Effect of aspect ratio on the elliptical entrainment coefficient β_e and the jet trajectory.

S	(1/SK^2)^1/3	βe
1	1.000	0.60
2	0.750	0.65
3	0.606	0.73
5	0.445	0.89
10	0.291	1.21
15	0.224	1.46
20	0.186	1.67
50	0.102	2.62

Appendix C

Derivation of Equation 4.9

Equation 4.9 is derived through the use of a control volume analysis using the control volume shown in Figure C.1. Equation 4.9 calculates the momentum of the jet issuing vertically from the top of the step based on the momentum of the fluid issuing horizontally from the jet tube.

Examining section A, the horizontal momentum balance can be determined assuming constant fluid density:

$$\rho V_1^2 A_1 = \frac{1}{2}\rho C_{DA} A_1 V_1^2 + \rho V_A^2 A_A \tag{C.1}$$

Examining section B, the horizontal and vertical momentum balances can be determined:

$$\rho V_A^2 A_A = P_A A_A \tag{C.2}$$

$$P_B A_B = \rho V_B^2 A_B \tag{C.3}$$

Assuming that side boundaries of region B follow constant pressure streamlines:

$$P_A = P_B \tag{C.4}$$

This yields:

$$V_A^2 = V_B^2 \tag{C.5}$$

Incorporating this into the conservation of mass equation along constant pressure streamlines yields:

$$A_A = A_B \tag{C.6}$$

The momentum conservation analysis for section C can then be determined:

$$\rho V_B^2 A_B = \frac{1}{2}\rho C_{DB} V_B^2 A_B + \rho V_2^2 A_2 \tag{C.7}$$

Using Equation C.5 and C.6 and combining Equations C.1 and C.7 yields:

$$\rho V_1^2 A_1 = \frac{1}{2}\rho C_{DA} V_1^2 A_1 + \frac{1}{2}\rho C_{DB} V_B^2 A_B + \rho V_2^2 A_2^2 \tag{C.8}$$

Then, defining the drag coefficient C_D:

$$\frac{1}{2}\rho C_D A_1 V_1^2 = \frac{1}{2}\rho C_{DA} A_1 V_1^2 + \frac{1}{2}\rho C_{DB} V_B^2 A_B \tag{C.9}$$

Incorporating Equation C.9 into Equation C.8 yields Equation 4.9:

$$\rho V_1^2 A_1 = \frac{1}{2}\rho C_D A_1 V_1^2 + \rho V_2^2 A_2 \tag{C.10}$$

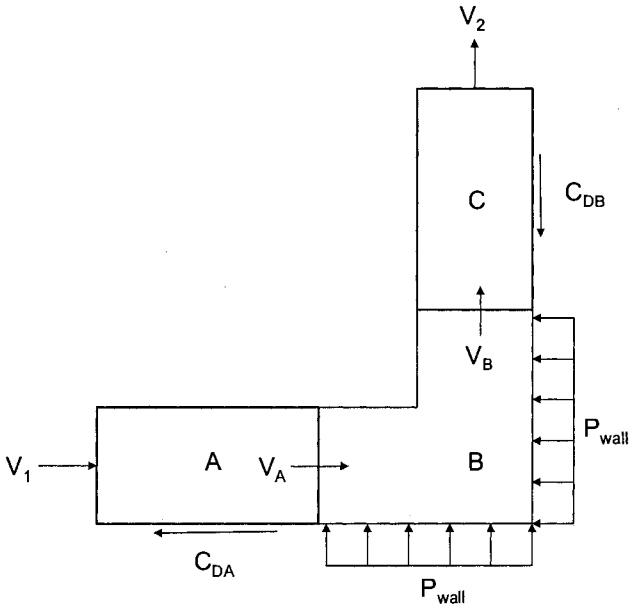

Figure C.1: Control volume for derivation of Equation 4.9

Appendix D

$L_\circ$ Independence in Trajectory Correlations

The correlation for the perimeter of the jet based on the velocity ratio, the step height, the distance from the jet to the step and the initial jet diameter is given in Equation 3.5. For large values of R or $\frac{HL_o}{d^2}$, this equation can be simplified to:

$$P \sim R^{0.2} H^{1/2} L_o^{1/2} \tag{D.1}$$

When this is substituted into the equations representing the jet trajectory in the near field region (Equation 4.1) and the bent-over region (Equation 4.3) with their fit coefficients the resultant equations are shown below:

Near field region:

$$h \sim R^{0.6} \left(\frac{d}{H}\right)^{1/4} d^{1/2} x^{1/2} \tag{D.2}$$

Bent-over region:

$$h \sim R^{0.713} \frac{d^{0.870} L_o^{0.043}}{H^{0.247}} x^{1/3} \tag{D.3}$$

Typically underground pipeline ruptures have very high velocity ratios. It is apparent from the correlations shown here (Equations D.2 and D.3) that the distance from the jet inlet to the step has very little effect on the jet's trajectory for high velocity ratios. In the near field region the term is removed from the equation for the jet's trajectory (shown in Equation D.2). In the far field region the exponent is nearly an order of magnitude smaller than the other terms (shown in Equation D.3). Thus, for the case of crater released jets, the diameter of the crater formed by the rupture is unimportant when determining the jet's trajectory.